DIPLOMARBEIT

Flexible Coil Arrays for Magnetic Resonance Imaging – Performance Comparison of Coaxial Transmission Line Resonators and Stranded Wire Elements

zur Erlangung des akademischen Grades

Diplom-Ingenieurin

im Rahmen des Studiums

Biomedical Engineering

eingereicht von

Raphaela Czerny
Matrikelnummer 01616248

ausgeführt am Atominstitut
der Fakultät für Physik der Technischen Universität Wien
in Zusammenarbeit mit dem Hochfeld MR Zentrum, Zentrum für Medizinische Physik und Biomedizinische Technik, Medizinische Universität Wien

Betreuung
Betreuer: Em. Univ. Prof. Dipl.-Ing. Dr.techn. Gerald Badurek
Mitwirkung: Assoc. Prof. Dipl.-Ing. Dr. Elmar Laistler

Wien, 13.05.2022

Raphaela Czerny

Gerald Badurek

Table of Contents

Abstract

Magnetic resonance imaging (MRI) is a non-ionizing medical imaging technique, based on the ability of certain atomic nuclei to interact with externally applied magnetic fields. Image quality is strongly determined by the receive sensitivity of the radiofrequency coils, used to pick up the MR signal emitted from the measured body region, among other factors like strength of the static magnetic field. Coil sensitivity can be greatly enhanced by proximity to the body, which can be achieved using flexible receive coils, enabling close form-fitting to arbitrary body shapes.

In this thesis a comparative study between flexible receive-only stranded wire coils and coaxial coils for magnetic resonance imaging at 3T is presented. The focus lies on the development process of a 4-channel stranded wire coil array. Stranded wire coils (SWC) were chosen due to their similar behavior to standard copper loop coils (SC). Their resonance frequency is determined by the inductance determined by the conductor geometry and capacitors along the conductor. Coaxial coils (CC) are self-resonant transmission line resonators, which are tuned by their geometry and cable characteristics.

Single channel coils and individual interfacing circuitries were constructed with rigid copper wire, flexible stranded wire, and flexible coaxial cables. Bench tests using a vector network analyzer were conducted to verify tuning, impedance matching and the efficiency of the active detuning network. Lower unloaded Q-factors were found for the coaxial coil, indicating higher coil losses. Nevertheless, all coils were clearly sample noise dominated. Bench measurements of the three coils showed robustness against bending in terms of frequency shifting, which was below 3 %. The MR measurements showed that the flexible SWC and CC only had slight signal-to-noise ratio (SNR) disadvantages against the rigid SC in a circular ROI on a flat phantom.

A 4-channel stranded wire coil was constructed, tested, and compared to a 4-channel coaxial coil. Similar geometric and preamplifier decoupling was found between the arrays. The MR measurements of the 4-channel coils included gradient echo, flip angle and noise scans. Considering that different preamplifiers were used, similar SNR was found in the defined region of interest for the two arrays. Therefore, other criteria than SNR performance should be considered for the choice between the two coil designs. These include the mechanical robustness against bending, where the CC outperforms the SWC as no additional solder joints along the conductor are required.

Danksagung

Ich möchte an dieser Stelle einer Reihe an Leuten danken, die mich während meiner Masterarbeit unterstützt und motiviert haben, und dazu beigetragen haben, dass ich diese Zeit so schön in Erinnerung habe!

Ein großes Dankeschön möchte ich Elmar Laistler ausrichten, der mir so viel über RF Engineering und MRI beigebracht hat, und vor allem seine Begeisterung dafür mit mir geteilt hat. Gerald Badurek möchte ich danken, der die Betreuung dieser Arbeit an der TU Wien übernommen hat.

Großer Dank gilt auch Lena Nohava und Michael Obermann, die mir oftmals mit Tipps und Ratschlägen helfend zur Seite gestanden sind und mir so vieles über RF Coils erklärt haben. Ich möchte mich auch bei allen anderen aus der Gruppe bedanken wie Sigrun Roat, Jürgen Sieg und Roberta Frass-Kriegl, weil sie mir nicht nur bei allen möglichen Fragen weitergeholfen haben, sondern mich auch so herzlich in ihr Team aufgenommen haben.

Als nächstes möchte ich meinen Freund Tobias erwähnen, der mich so oft motiviert hat und dem ich auch in stressigeren Wochen viele schöne und lustige Abende zu verdanken habe. Meiner Schwester Katharina möchte ich danken, dass sie immer ein offenes Ohr für mich hat und mich gemeinsam mit meinen Eltern Martina und Thomas schon seit Beginn des Studiums unterstützt.

Danke schön an alle!

1 Introduction

Magnetic resonance imaging

Magnetic resonance imaging (MRI) presents a diagnostic procedure in radiology, generating images of the human anatomy and revealing detailed tissue structures. This medical imaging method is non-ionizing in contrast to other techniques like X-ray examinations, computed tomography (CT) and positron emission tomography (PET) scans. The foundation of MRI is represented by nuclear magnetic resonance (NMR) describing a physical phenomenon discovered by Rabi *et al*. [1] in the 1930s in molecular beams as an extension of the Stern-Gerlach experiment. In 1946 Bloch [2] and Purcell [3] were able to expand this concept, demonstrating a method to determine the molecular structure in solids and liquids. The technique exploits the behavior of magnetic moments of nuclei, which is assembled by the nuclear spin, to align to an external magnetic field. Only certain atomic nuclei are suited for these experiments, as non-zero nuclear spins are required. In medicine, hydrogen atoms are usually used for MRI, present in large quantities in the human body. In the bore of an MR scanner a high static magnetic field is typically generated by superconducting coils, interacting with the magnetic moments and enforcing a precession about the field axis. Supplementary coils, emitting additional electromagnetic fields oscillating at the precession frequency in the radio frequency (RF) range, hence called "RF coils", deflect the magnetic moments from their alignment. Subsequently, the absorbed energy is emitted by the nuclei and enables the reception of MR signal via the RF coil, often the same coil used for transmission. For receive sensitivity enhancement a supplementary receive coil can be employed in addition to the transmit coil [4].

Flexible radio frequency coils

The design of an RF coil plays an essential role in improving the achievable signal-to-noise ratio (SNR), as it influences the interaction between coil and body. Proximity to the measured body part enhances the receive sensitivity of the coil due to stronger magnetic coupling. As flexible coil elements allow for form-fitting RF coils, various flexible or stretchable coil design approaches have been studied recently. Especially biomedical applications with high inter-patient variability, *e.g.*, imaging of the abdomen or the breast, are benefitting from coils which are able to adapt to the shape of the measured body part. Additional data quality improvement can be accomplished by exploiting signal-to-noise ratio enhancement of coil arrays, phased arrays as well as parallel imaging methods [5,6].

Motivation of the thesis

The motivation of this thesis was to construct an RF coil array made from stranded wire and compare it to an existing coaxial coil array, both made from flexible and light-weight cables. They will be designed as receive-only coil arrays for MRI at 3 T and consist of 4 channels (ch).

This coil design comparison was chosen, as both designs offer flexibility while showing different electromagnetic properties. Stranded wire coils show similar behavior to standard copper loop coils. The same coil interface structure can be used and tuning of coil to the desired resonance frequency is accomplished by capacitors along the conductor. Coaxial coils with a gap in the outer and inner conductor, on the other hand, are self-resonant transmission line resonators. They are tuned by their geometric properties and therefore do not require additional electrical components on the loop itself. In addition to the comparison of the 4-channel coil arrays, single element coils, made from stranded wire, coaxial cable and rigid copper were fabricated and measured on the bench and in the MR scanner. The focus lies on the construction process of the flexible stranded wire coil array and its interfacing circuitry. Similar properties of the two arrays (*e.g.*, size, flexibility, coil arrangement and overlap) will be chosen for better analysis. Studying the behavior of both coil array designs, their performance will be evaluated by bench and MR measurements. Different coil parameters, such as inter-element coupling, Q-factor, SNR, noise correlation and g-factor, will be measured and calculated in the course of this study.

The 4-channel coaxial coil will be integrated into a 28-channel receive-only coil array for the imaging of the breast at 3 T, the so-called Bracoil. This bra-shaped RF coil will have a form-fitting and light-weight design, requiring flexible coil elements. This ongoing project intends to represent an alternative to X-ray mammography, improving the currently used method in breast MRI. This will be achieved by higher sensitivity and specificity enabled by the shape-adapting design and increased patient comfort due to shorter measurement times and the flexible and light-weight RF coil as well as integrated motion correction. The results of the comparative study in this work will help to decide on the coil type, which is better fitted for this specific application.

2 Theoretical background

This Chapter covers the theoretical principles underlying the development of RF coils constructed in this thesis. In the first Section, the physical laws and processes behind the nuclear resonance phenomenon, forming the basis of MR imaging, are discussed. The second Section focuses on the electromagnetic basics of RF coils and gives a brief overview on different coil designs and the evaluation of coil performance.

2.1 Magnetic resonance imaging

2.1.1 Nuclear spin

The phenomenon of nuclear magnetic resonance originates from the intrinsic angular momentum $\boldsymbol{I}$ of atomic nuclei. This so-called nuclear spin is composed of the intrinsic and orbital angular momenta of the nucleons, the protons and neutrons of the nucleus, determining its total magnitude. The postulates of quantum mechanics demand the quantization of the nuclear spin, thus definite discrete values are possible.

$$|\boldsymbol{I}| = \sqrt{I(I+1)}\hbar, \qquad 2.1$$

with the nuclear spin quantum number I being an integer, half-integer or zero, and the reduced Planck constant $\hbar$.

The projection on the quantization axis (here: z-axis) is described by the nuclear magnetic quantum number m_I.

$$I_Z = m_I \hbar, \qquad 2.2$$

with m_I ranging from $-I,\ -I+1, \dots,\ I-1,\ I$, allowing $2I+1$ possible configurations.

As fermions, protons and neutrons have a nuclear spin of $I = \frac{1}{2}$, limiting the potential values of m_I to $\pm\frac{1}{2}$, which is the case for hydrogen atoms (^{1}H). Nuclei with a non-zero angular momentum have a magnetic moment μ. The two characteristic parameters of the nucleus I and μ are linked by a parameter – the gyromagnetic ratio γ, which describes the ratio of magnetic to angular momentum.

$$\mu = \gamma \boldsymbol{I}, \quad \text{with} \quad \gamma = \frac{g_I\, \mu_N}{\hbar}, \qquad 2.3$$

with the characteristic nuclear g-factor g_I and the nuclear magneton μ_N which can be derived in an analog way as the Bohr magneton [7].

Due to the complex pairing of protons or neutrons, every nucleus with an odd number of one or both nucleons (so an unpaired nucleon) possesses a magnetic moment which is required for nuclear magnetic resonance. MR spectroscopy measurements can be constructed for the detection of magnetic resonance of different atomic nuclei, however for imaging experiments the hydrogen atom is by far the most common used nucleus. This is due to its high gyromagnetic ratio compared to other stable nuclei and its high natural abundance in biological systems, which implies a strong MR signal of the sample [8,9]. In Tab. 2.1 the characteristics of several nuclei, which are frequently used in MR imaging and spectroscopy, are listed.

nucleus	Z	I	γ **[MHz/T]**
^{1}H	1	1/2	42.6
^{2}H	1	1	6.5
^{13}C	6	1/2	10.7
^{19}F	9	1/2	40.1
^{23}Na	11	3/2	11.3
^{31}P	15	1/2	17.3

Tab. 2.1: Isotopes frequently used in magnetic resonance experiments and their nuclear properties: atomic number Z, quantum number I and gyromagnetic ratio γ [8].

2.1.2 Alignment and precession

Magnetic resonance imaging requires a high magnetic field. The exposure to an external magnetic field results in a disturbance of the random orientation of the magnetic moments of the nuclei in the measured sample. It is caused by a torque forcing the magnetic moments to align parallel to the magnetic field lines. The static magnetic field $\boldsymbol{B}_0$, generated by superconducting coils in the bore of the MR scanner, only has a component in z-direction.

A magnetic moment has the potential energy E when applying an external magnetic field (using Eqs. 2.2 and 2.3), where

$$E = -\mu \boldsymbol{B}_0 = -\gamma m_I \hbar \boldsymbol{B}_0. \qquad 2.4$$

Depending on the orientation of their magnetic moments, the spins align either parallel or antiparallel to the z-axis of the magnetic field and start precessing about this axis at the so-called Larmor frequency ω_L. These configurations have different potential energy because of numerous possible m_I values. The splitting of the degenerate energy levels in $2I + 1$ different states is caused by the Zeeman effect [7] and is shown in Fig. 2.1.

Only a transition of $\Delta m = \pm 1$ is allowed, consistent with the selection rules of quantum mechanics. The energy difference between two arbitrary neighboring states is equidistant and is described by the following equation

$$\Delta E = \gamma\hbar\boldsymbol{B}_0. \tag{2.5}$$

This amount of energy is necessary for an elevation to a higher state by the absorption of photons. A transition of the nuclear spin levels can be induced by excitation at the Larmor frequency ω_L , which corresponds to the energy difference ΔE, given by

$$\Delta E = \hbar\omega_L, \tag{2.6}$$

$$\omega_L = \gamma\boldsymbol{B}_0. \tag{2.7}$$

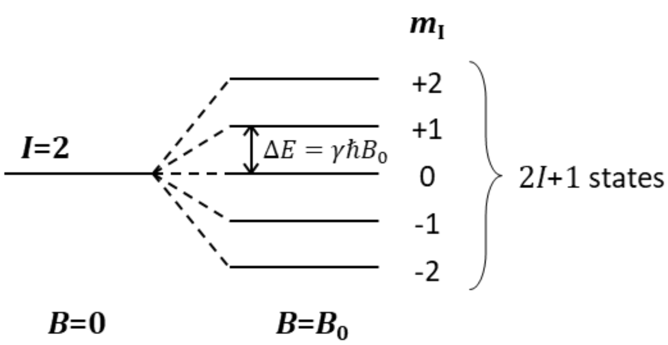

Fig. 2.1: Splitting of the spectral lines when applying an external magnetic field B due to the Zeeman effect with nuclear spin I and nuclear magnetic quantum number m_I, [7].

When a sample is exposed to a static magnetic field $\boldsymbol{B}_0$ in z-direction, its nuclear magnetic moments undergo Larmor precession around the z-axis. A minimal surplus of magnetic moments aligns parallel, as the nuclei are reaching for the lowest energy level. This results in a small macroscopic magnetization in positive z-direction which is essential for the detection of an MR signal. Only this small amount contributes to the total nuclear magnetization $\boldsymbol{M}$ as the rest of them cancels each other out, shown in Fig. 2.2 [8].

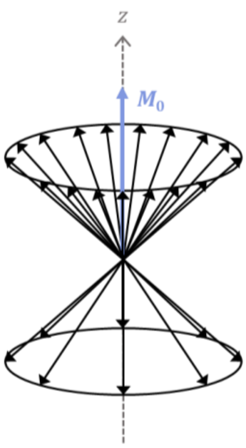

Fig. 2.2: The nuclear magnetization $\boldsymbol{M}_0$ of a fermion system (*e.g.*, ^{1}H nuclei): higher occupation in the spin precession cone of lower energy state with magnetic quantum number $m = +\frac{1}{2}$ (parallel alignment to $\boldsymbol{B}_0$) [8].

In thermal equilibrium, the unequally distributed spin populations of hydrogen nuclei in a sample are following Boltzmann statistics,

$$\frac{N_{\uparrow\downarrow}}{N_{\uparrow\uparrow}} = e^{-\frac{\Delta E}{k_B T}} = e^{-\frac{\gamma\hbar \boldsymbol{B}_0}{k_B T}}, \qquad 2.8$$

with the Boltzmann constant k_B and the temperature T [7].

2.1.3 Excitation and relaxation

For the detection of an electromagnetic signal from the sample an excitation of the nuclear spins, as mentioned in the previous Subsection, is necessary. This needs to occur at the resonance frequency $f_L = \frac{\omega_L}{2\pi}$, which is determined by the nucleus of interest and the static magnetic field strength of the MR scanner. Standard magnetic field strengths and their respective resonance frequency of hydrogen nuclei are listed in Tab. 2.2.

$\boldsymbol{B}_0$ **[T]**	1.5	3	7
f_L **[MHz]**	63.9	127.7	298.1

Tab. 2.2: Magnetic field strengths $\boldsymbol{B}_0$ of MR scanners with the corresponding resonance frequency f_L of ^{1}H.

These RF pulses are generated by the so-called RF coils producing an additional magnetic field $\boldsymbol{B}_1$. This time-dependent field is perpendicular to $\boldsymbol{B}_0$, rotating in the x-y-plane at $\omega_L = 2\pi f_L$. The interaction between the total magnetic field and the precessing nuclear magnetization over time can be described by the Bloch equation (in vector notation), where $\boldsymbol{M}$ is composed of all magnetic moments in the sample.

$$\frac{d\boldsymbol{M}}{dt} = \gamma \boldsymbol{M} \times \boldsymbol{B}(t), \qquad 2.9$$

$$\text{with } \boldsymbol{B}(t) = \begin{pmatrix} B_{1x}(t) \\ B_{1y}(t) \\ B_0 \end{pmatrix}.$$

Multiple RF pulses varying *e.g.*, in duration, amplitude and phase are compiled in so-called pulse sequences. The adjustments enable the adaption of the flip angle and excitation profile of the deflection of magnetic moments from their original magnetic alignment with $\boldsymbol{B}_0$ into the transverse plane. This is essential for the regulation of the contrast of the image for example due to different T_1- and T_2-weighing.

After excitation, the nuclei strive to return to their equilibrium state by relaxation processes. They are characterized by material-dependent relaxation times that determine the contrast of the obtained image. Two independent processes can be distinguished, called “spin-lattice” and “spin-spin relaxation”, which will be described next.

Spin-lattice interaction

The longitudinal relaxation results in the recovering of the spin alignment along the z-axis of the static magnetic field $\boldsymbol{B}_0$. Energy is transferred to the molecular lattice of the sample, converting it into heat. The time constant T_1 is linked to the process as follows

$$M_z(t) = M_z(0) \cdot (1 - e^{-\frac{t}{T_1}}). \tag{2.10}$$

Spin-spin interaction

The transverse relaxation describes the decay of magnetization in the x-y-plane induced by the orthogonal RF pulses. It is the result of the dephasing of the spins, without energy exchange with the environment. This relaxation proceeds faster than the recovery of the longitudinal magnetization. After the time T_2, the amplitude of the deflected signal decreases to $\frac{1}{e}$ of the initial value. Thus, the interaction can be described by an exponential decay,

$$M_{x,y}(t) = M_{x,y}(0) \cdot e^{-\frac{t}{T_2}}. \tag{2.11}$$

Bloch equations

When considering the influence of relaxation processes on the magnetization, as the perturbed magnetic moments strive for thermal equilibrium, the Bloch equations in the laboratory frame must be adapted in the following way.

$$\begin{aligned}
\frac{dM_x}{dt} &= \gamma\left(M_y B_0 - M_z B_{1y}\right) - \frac{M_x}{T_2}, \\
\frac{dM_y}{dt} &= -\gamma(M_x B_0 - M_z B_{1x}) - \frac{M_y}{T_2}, \\
\frac{dM_z}{dt} &= \gamma\left(M_x B_{1y} - M_y B_{1x}\right) - \frac{M_z - M_0}{T_1}.
\end{aligned} \tag{2.12}$$

After excitation, the precession of the magnetization is detected by the RF coils via electromagnetic induction [10,4], which will be explained in detail in the following Section 2.2.

2.2 Radio frequency coils

RF coils generate the $\boldsymbol{B}_1$ transmit field and receive the magnetic resonance signal from the sample. Transmit (Tx) and receive (Rx) coils can be distinguished, however it is also possible to merge these functions into transceiver (Tx/Rx) coils. This combination is often embedded in the scanner itself functioning as a so-called body coil, covering a length of ca. 50 cm in z-direction. For ultra-high magnetic field strengths (7 T and above), local transmit coils are required as integrated body coils with homogeneous excitation patterns are not feasible as a consequence of complex RF-body interactions at the high frequency. Up to 3 T, MR scanners usually have built-in Tx/Rx body coils, however additional Rx only coil arrays are commonly used as they enable higher acquisition speed and SNR [9].

RF coils are electric circuits resonating at the Larmor frequency of the examined nuclei. The coils are connected to a receiver chain, enabling the transmission and processing of detected signals by an electronic network [8]. The network, which is used in the scope of this thesis, consists of a tuning and matching stage, an active detuning circuit, a Balun (balanced-unbalanced conversion), phase shifter, and preamplifier. The following Sections give detailed information on the process of signal reception, the resonance of electrical circuits and the interfacing circuitry of RF coils. Furthermore, different RF coil designs and their performance evaluation are discussed.

2.2.1 Signal reception

The magnetic flux Φ_m is described by the magnetic field $\boldsymbol{B}$, also called magnetic flux density, passing through a surface A, defined by the following surface integral

$$\Phi_m = \int_A \boldsymbol{B} \cdot dA. \tag{2.12}$$

If a sample is exposed to RF pulses, the subsequent deflection of magnetic moments causes a change of the local magnetization. The transmitted electromagnetic energy flips the longitudinal magnetization M_0 into the transverse plane where it forms the macroscopic magnetization M_{xy}. This process is shown in Fig. 2.3 for a 90° pulse irradiation forcing the magnetic moments of the measured nuclei to a synchronization of their phases.

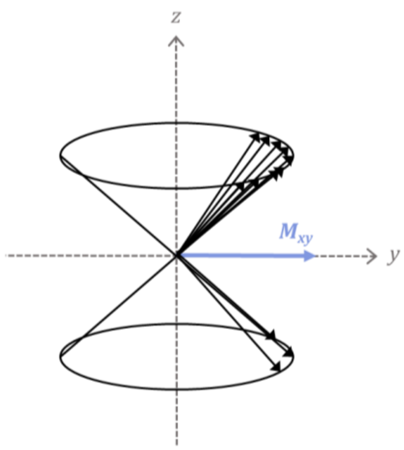

Fig. 2.3: Induced phase coherence of the magnetic moments μ, which were originally aligned along the z-axis in direction of the static magnetic field B_0, caused by a 90° RF pulse resulting in a macroscopic transverse magnetization M_{xy} [8].

When an RF coil is placed on this sample, the magnetic flux through the coil area A is changed. According to Faraday's law of inductance this alternation induces a voltage U_{ind} (equivalent to an electromotive force ε) across an electrical conductor,

$$\frac{d\Phi_m}{dt} = \frac{d}{dt}\int \boldsymbol{B} \cdot dA = -U_{ind}. \tag{2.13}$$

This relation can also be described by Maxwell's equation (using Stokes' theorem) – a change of the magnetic field lines through a surface induces an electric field $\boldsymbol{E}$ in the conducting loop of the RF coil,

$$\int_A \frac{\partial \boldsymbol{B}}{\partial t} \cdot dA = -\oint_{\partial A} \boldsymbol{E} \cdot ds. \tag{2.14}$$

The induced difference in electric potential is in relation with the rate of change of current with the proportionality factor L called inductance of a coil,

$$U_{ind} = -L\frac{dI}{dt}. \tag{2.15}$$

These currents can be detected and represent the MR signal which is proportional to the induced alternating voltage. Spatial localization is accomplished by supplementary field gradient coils in the bore of the scanner. They are superimposed on the main static field $\boldsymbol{B}_0$ and make the precession frequency and phase dependent on position. This complex gradient system allows for 3-dimensional spatial encoding [9,10]. For the reconstruction of an image, the received signals are amplified, filtered and digitalized for data analysis. Afterwards they are fed to the computer of the MR system for further signal processing [11,12]. MR signals are acquired as data points in the k-space, therefore a Fourier transform is applied to reconstruct the image. A more thorough discussion on the complex process of image reconstruction can be found in [4].

2.2.2 RLC circuit

Radio frequency coils consist of an inductance L from the coil itself, a resistance R from the wire losses (and soldering joints) and a capacitance C, which is typically added to the circuit by soldering capacitors into the circuit (for the case of standard or stranded wire coils, see Subsection 2.2.7). These components together form a RLC resonator oscillating at its resonance frequency which can be influenced by the choice of the capacitors (see Subsection 2.2.3). The oscillation originates from the alternating charging and discharging of the capacitor, which causes currents of opposite directions generating a magnetic field in the inductance. This process is periodic at the resonance frequency [11].

The impedance of a series resonant circuit is calculated by the following equations [11]

$$Z(\omega) = R + iX, \tag{2.16}$$

with $X(\omega) = X_L + X_C = \omega L - \frac{1}{\omega C}$.

To detect the induced signal from a sample during an MR experiment, the voltage is picked up at the coil port and the signal is further transmitted to the receiver chain. Therefore, the RF antenna represents a parallel resonant circuit as shown in Fig. 2.4.

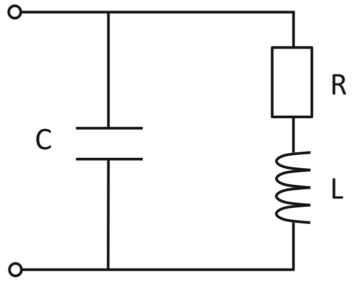

Fig. 2.4: Electric circuit diagram of an RF coil: parallel RLC resonant circuit with resistance R, inductance L, and capacitance C.

The respective impedance of this circuit type can be derived by the reciprocal value of Eq. 2.22 [11],

$$\frac{1}{Z(\omega)} = \frac{1}{R + i\omega L} + i\omega C. \tag{2.17}$$

2.2.3 Tuning and matching

The RF antenna needs to resonate precisely at the Larmor frequency to achieve optimal performance. During the process of tuning, where the coils are set to the desired frequency, a capacitance C is added to the electric circuit, so far consisting solely of a wire loop (L + R). When approaching the resonance frequency ω_0, the imaginary part of the impedance Z, the reactance X, disappears.

$$Z(\omega_0) = R \;\; \Rightarrow \;\; X(\omega_0) = 0. \tag{2.18}$$

Eq. 2.18 describes the impedance where the resonance condition is met. The behavior of the impedance at f_0 is also shown in Fig. 2.5 for the parallel circuit.

Another aspect must be considered when tuning the coil which is the segmenting of the coil, creating a more even current distribution along the conductor. For this purpose, the wire loop is segmented by capacitors as demonstrated in Fig. 2.6. They are soldered into the coil, connecting the capacitors in series. The length of one coil segment should not exceed a certain limit, determined by the corresponding wavelength λ at the operating frequency. Typically, this segment length should be chosen between $\lambda/20$ and $\lambda/10$. The segmentation prohibits the development of standing waves in the coil loop. These destructive electromagnetic interferences in the center of the coil are suppressed because of the phase shift caused by the capacitances. Also, using this method the magnitude of the electric field is decreased, thereby reducing sample losses and heating of the sample [13,14].

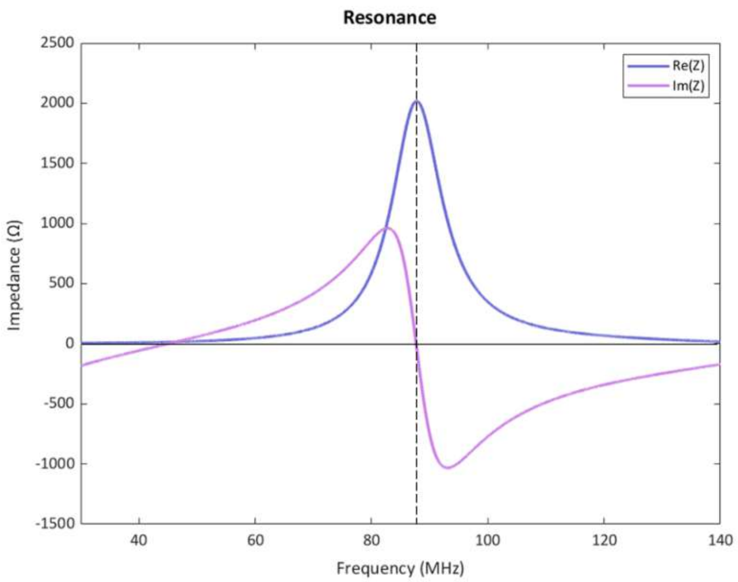

Fig. 2.5: Parallel resonant circuit: real (blue) and imaginary (violet) part of the impedance $Z = R + iX$ dependent on the frequency (resonance at f_0: dotted line).

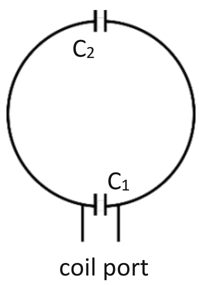

Fig. 2.6: Standard radio frequency coil which is segmented by two tuning capacitors C_1 and C_2. C_1 is located at the RF coil port.

For optimal SNR, the MR signal which is picked up by the RF coil is fed into a preamplifier as close to the coil as possible. To prevent additional signal loss due to reflections, the coil's impedance must be matched to the preamplifier and the rest of the receive chain. Commonly used preamplifiers and coaxial cables, presenting the subsequent connection to the scanner, have a characteristic impedance of 50 Ω [15].

2.2.4 Active detuning

When operating with receive-only RF coils, the transmit field originates from a supplementary Tx coil, in most cases the body coil of the scanner. This requires efficient detuning of the Rx coils during the process of transmission to prevent any interaction between the Tx and Rx coils. If not properly decoupled, the electromagnetic field can be concentrated by the Rx coils potentially leading to a risk of burns to the patient and impairment the measurement results. Also, electrical components like the preamplifier could be destroyed when exposed to the transmission signal. Decoupling can be realized by an active detuning (AD) circuit operating at the same frequency as the RF coil which forces the splitting of the f_0 peak due to mutual inductance. As a result, the Rx coils present a high impedance at f_0, preventing current from flowing in the Rx coils [15].

An active detuning circuit for a stranded wire or standard RF coil (see Subsection 2.2.7) consists of a capacitance, an inductance and a PIN-diode connected to a direct current (DC). Only in reception mode the Rx coil is resonant, while at all other times the active detuning circuit is resonant, *i.e.* the Rx coil is in the detuned state. The DC signal is isolated from the remaining components of the RF coil by blocking capacitors with high capacitance, which present a low impedance for high frequencies and an open circuit for DC. Conversely, to prevent high frequency currents from entering the DC part of the circuit, two RF choke inductors are integrated in the network.

A slightly different technique is applied for the detuning of coaxial RF coils. The resonance of these coils is not split but instead completely destroyed by shorting the inner and outer conductor of the coaxial cable at the coil port, resulting in high impedance of the coil at the Larmor frequency. Again, the detuning is controlled by a DC interconnecting a PIN diode leading to a short between the two conductors. The two mentioned active detuning networks are shown in a circuit diagram in Fig. 2.7.

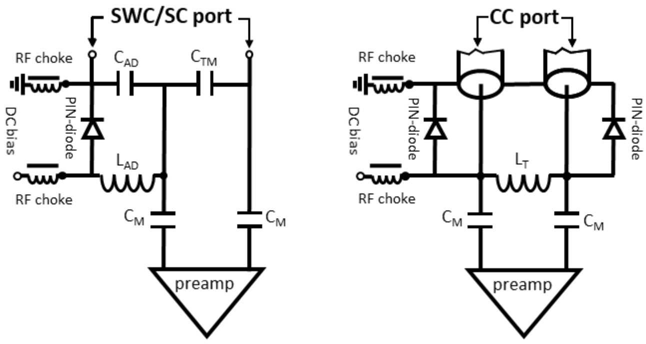

Fig. 2.7: Tuning (L_T, C_{TM}), matching (C_M), and active detuning network (PIN-diodes, RF chokes, C_{AD}, L_{AD}) of a coaxial coil (left) and a standard or stranded wire coil (right) with preamplifier [16].

2.2.5 Balun

The RF coil is connected to the receiver by an electrically asymmetric coaxial cable. Since the electrically balanced Rx coil is connected to an unbalanced transmission line, a Balun transformer is necessary to avoid common mode currents. A balanced signal consists of two inversely phased alternating voltages of the same amplitude oscillating against ground. On the contrary, in an unbalanced line, a single alternating voltage works against ground accounting for an unequal impedance with respect to ground. A Balun prevents the flow of common mode currents on the outer surface of the coaxial cable at these high frequencies. These currents could result in an additional loss source or influence tuning and matching. A feasible transformer for this application would be a LC-Balun, consisting of a bridge with two capacitors and two coils of the same capacitance and inductance opposite to each other. Furthermore, the circuit acts as an impedance matching stage. The described Balun transformer can be seen in Fig. 2.8 [17].

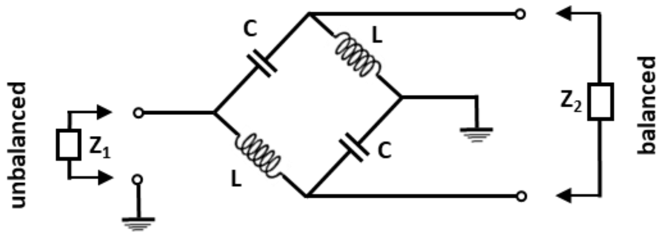

Fig. 2.8: Circuit diagram of a LC-Balun (balanced to unbalanced line transformer) which is formed by a bridge consisting of two capacitances C and two inductances L [17].

The following relation between the inductors L, capacitors C and the impedances $Z_1$and Z_2 ($\triangleq Z_0$), which are shown in Fig. 2.8, applies [17]

$$\omega_0 L = \frac{1}{\omega_0 C} = \sqrt{R_1 R_2}\,. \tag{2.19}$$

2.2.6 Inter-element decoupling

When implementing the RF coils in array configuration, it is essential to achieve sufficient decoupling between the coil elements. Otherwise, the magnetic flux of the resonant circuits would interact with each other leading to a perturbing induction from one coil to the other. A splitting of the resonance frequency peak of the coil can be observed as a result. This mutual induction would degrade the sensitivity of the array [17].

The magnitude of this electromagnetic interaction can be described by the coupling coefficient k [10],

$$k = \frac{M_{12}}{\sqrt{L_1 L_2}}, \tag{2.20}$$

defined by the mutual inductance M_{12} between coil 1 and coil 2 and their inductances L_1 and L_2.

2.2.6.1 Overlap decoupling

By geometrically arranging adjacent coils in a particular overlap configuration, it is possible to nullify the mutual induction of nearest neighbors [17,18]. This effect is achieved when the magnetic flux generated by one coil in the second coil is zero. This state is found only at a specific relative position of these coils where the integral of the magnetic flux over the area outside loop 1 within loop 2 is equal and of opposite sign to the integral of the magnetic flux over the overlapping area. The overlap for optimal decoupling strongly depends on the geometric shape of the coil. For two equally sized circular coils, the condition is fulfilled when the distance between the coil centers equals 0.78 times the coil diameter. An illustration of the effect can be seen in Fig. 2.9.

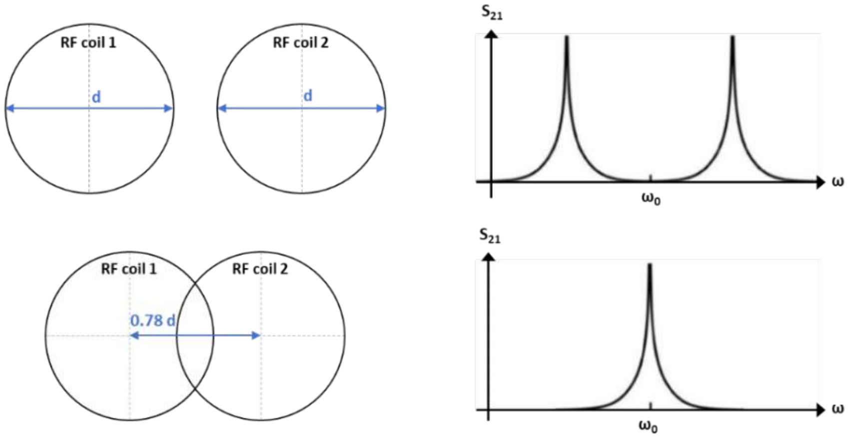

Fig. 2.9: Splitting of the resonance frequency peak due to mutual inductance of two coils (top) and optimal overlap with minimal coupling between the coils (bottom) [9].

2.2.6.2 Preamplifier decoupling

The remaining coupling between non-neighboring coils can be minimized by exploiting the technique of preamplifier decoupling. The basic idea of this principle is to transform the low input impedance of the preamplifier to a very high (infinite) impedance at the coil port. Thus, the coil sees an open circuit preventing currents from flowing in the coil. Since a magnetic flux can only exists when a current is flowing, this method suppresses mutual induction and, therefore, coupling. Simultaneously, the coil impedance needs to remain matched to the preamplifier input to achieve optimal SNR. The transformation is accomplished by the implementation of a phase shifter before the preamplifier which does not degrade the tuning or matching [18,19]. The desired impedances of the coil, the connecting circuitry and the preamplifier for ideal decoupling and matching can be seen in Fig. 2.10.

The desired shift can be calculated by the following equation, linking the impedance seen from the coil at the port $Z_{interface}$ with the matched impedance Z_0 [20].

$$Z_{interface} = iZ_0 \tan{(\beta l)}, \qquad 2.21$$

$$\text{with } \beta = \frac{2\pi}{\lambda}.$$

As a maximum of the impedance Z_{in} is desired, the optimal shift therefore needs to be $\frac{\pi}{2}$ ($\triangleq$ 90°) to avoid inductive coupling, which corresponds to an l of $\lambda/4$.

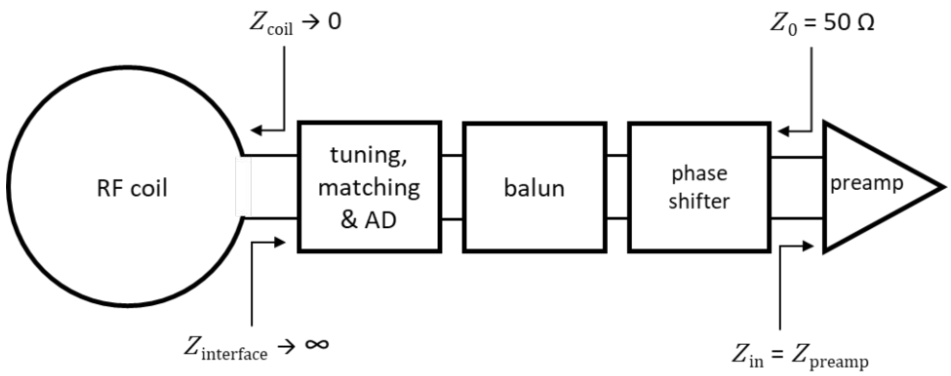

Fig. 2.10: Impedances Z of an optimal matched and decoupled RF coil interface at the coil port and between coil interface and preamplifier (seen from both directions) [19].

2.2.7 Coil designs

Radio frequency coils are not restricted to a certain type of design, a variety of RF coil types exists and is currently employed in MR experiments. Often, Rx and/or Tx coils are implemented in arrays, which will be discussed more thoroughly in Subsection 2.2.7.4. Depending on the specific biomedical application of the coil, the design varies to ensure optimal measurement results. The coils can differ for example in their shape, size or used wire/cable and choice of interface components. Two basic design types can be distinguished, which are volume and surface coils. Volume coils surround the measured sample or body part, allowing a large field of view (FOV), and generate a relatively homogeneous B_1 transmit field. Widespread volume coil designs are the TEM (transverse electromagnetic resonator) or the birdcage coil, like the in-built body coil used in most clinical MR scanners. On the contrary, surface coils are placed close to the ROI, gaining more sensitivity at the cost of a restricted volume coverage and decreasing B_1 homogeneity with larger distance to the coil. Hence, they are used to acquire high SNR images in a smaller FOV. They are adapted to the shape of the examined body part to enable a higher transmit efficiency and/or receive sensitivity in a region close to the coil. Typically, the two design approaches also differ in the size of their implemented coils since volume coils are usually constructed out of larger coils [21].

The following Subsection gives a small overview on several types of surface coil designs and their differences, focusing on the coils that were built and compared in this work.

2.2.7.1 Standard coils

Conventional coils are constructed from a copper wire arranged in a loop or rectangular shape. This winding is segmented by capacitors to achieve the desired resonance frequency. Lumped elements, which are soldered onto the coil, and the copper wire itself makes standard coils (SCs) rigid devices. The impedance at the coil port is low, therefore a high impedance is needed to achieve preamplifier decoupling [9].

2.2.7.2 Stranded wire coils

Radio frequency coils out of stranded wire behave similarly to standard coils in terms of electro-magnetic characteristics. This wire consists of single strands of thin copper wire twisted and bundled together surrounded by an isolation as shown in Fig. 2.11. The equivalent behavior to standard coils can be explained by the electrical connection of the strands. Therefore, stranded wire coils (SWCs) are low impedance coils as well and require tuning capacitors along the conductor. Equivalent interface structures as for SCs can be employed. The major difference compared to conventional coils is their mechanical flexibility. The advantages of flexible coils are discussed in Subsection 2.2.7.4.

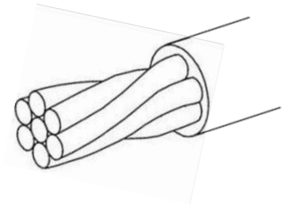

Fig. 2.11: Schematic drawing of a stranded wire: twisted copper strands surrounded by an insulator.

2.2.7.3 Transmission line resonators

Parallel-plate transmission line resonators

A different design approach, introduced by P. Gonord *et al.* [22,23], is the implementation of parallel-plate transmission line resonators (TLRs). This coil type has been employed and adapted in several other studies demonstrating high flexibility in array applications [24-26]. In [24], TLR coils are built by arranging two conducting bands on top of each other, a dielectric placed in between, shown in Fig. 2.12. Both conductors are segmented by one or more gaps and can consist of several turns [25], determining the inductance of the coil which depends on the inductor length. These structures are self-resonant and are tuned by geometric adaptation of the coil, hence eliminating the need for soldering lumped elements onto the coil itself. Their capacitance, defined by the permittivity used dielectric and its thickness, is distributed along the conductor, as opposed to the coils discussed in the previous Sections.

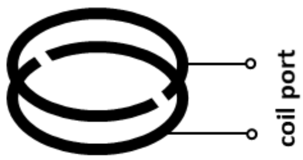

Fig. 2.12: Transmission line resonator: two conductors with one gap each, separated by a dielectric [9].

Coaxial transmission line resonators

Another variant of TLRs with a coaxial instead of a parallel-plate geometry was presented by B. Zhang *et al.* [27] and others [28-31]. Coaxial coils (CCs) made from regular non-magnetic coaxial cable are popular due to their high flexibility and robustness against loading variations, bending, and coil overlap. Similarly to the parallel-plate TLR, their resonance frequency is determined by the geometric characteristics (such as diameter or number of gaps and turns) and the dielectric and geometric properties of the used cable. A gap is realized by interrupting once the outer conductor and once the inner conductor at certain positions on the coil. These coils are, in contrast to standard and stranded wire coils, high impedance coils, hence for sufficient current suppression a low impedance at the coil port is needed. A comparison between a CC and SC/SWC can be seen in Fig. 2.13.

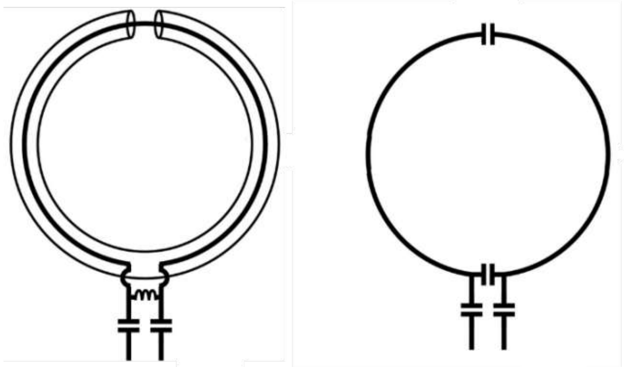

Fig. 2.13: RF coil designs: Coaxial coil (left) with a gap in the outer conductor and an inner gap at the coil port, fine-tuned by an inductor and matched by two capacitors. Standard/stranded wire coil (right) with a tuning and matching network.

2.2.7.4 Coil arrays

To improve image quality in MRI, small surface coils employed in phased arrays are favored over a single large coil [18]. With decreasing diameter, coils are more sensitive in the region they are covering, and less noise is detected due to the limited FOV. By the principle of reciprocity, the induced current rises with the minimization of the coil diameter due to a higher magnitude of the generated magnetic field, according to Biot-Savart's law [11]. Exploiting these effects, arrays of small coils enable higher SNR while allowing the same volume coverage. Furthermore, when additionally applying parallel imaging methods [32-34], the spatial variance of coil sensitivity patterns can be utilized to obtain spatial information. This partially spares the need for phase encoding via gradient coils, which is a time-consuming process, and thus allows for shorter acquisition times.

2.2.7.5 Flexible coils

In MRI experiments, proximity to the measured body part is essential for high magnetic coupling. This enhances receive sensitivity, which weakens with distance, and results in a decreasing variation of loading conditions. Therefore, flexible coils are a major advantage as they can be adapted to an arbitrary shape or structure. [9] Form-fitting coils are especially beneficial in applications with high inter-patient variability. Hence, flexible or stretchable RF coils and coil array design approaches are studied extensively. Examples include braided conductors [35], liquid metal filled tubes [36], CC arrays [37,6], multi-turn multi-gap CCs [16] or SWC arrays [38].

2.2.8 Performance measures

Several parameters are used to evaluate the performance and quality of the RF coil array. These include Q-factor and Q-ratio of the coil, the achievable signal-to-noise ratio (SNR) in an MRI experiment, g-factor and noise correlation matrix.

2.2.8.1 Q-factor and Q-ratio

For the evaluation of the energy loss of RF coils, the Q-factor can be determined, described by the following equation

$$Q = \frac{\omega_0 L}{R} = \frac{1}{\omega_0 C R}. \quad 2.22$$

with $R = R_C + R_S$. The total resistance R is composed of losses originating from the coil and sample. The coil resistance R_C increases by the square root of the frequency due to the skin effect. In contrast, the resistance of the sample R_S increases quadratically with frequency. This is the result of magnetic coupling generated by the Brownian motion of electrically charged particles causing randomly fluctuating magnetizations [14].

The Q-ratio provides a measure for the deviation of the coil and sample resistance. It represents the ratio of the Q-factor of the unloaded (without a sample) to the loaded measurement,

$$Q\text{-}ratio = \frac{Q_U}{Q_L} = \frac{R_C + R_S}{R_C} = 1 + \frac{R_S}{R_C}. \quad 2.23$$

Ideally, the RF coil operates in the sample noise domain indicating negligible coil losses which is the case for Q-ratios well above 2, *i.e.* $R_S >> R_C$. This implies that the measurement quality is limited by the loss contribution of the sample (which cannot be avoided) instead of the coil itself [15].

2.2.8.2 Signal-to-Noise Ratio (SNR)

An important parameter regarding the quality of the MR measurement is the signal-to-noise ratio. It determines whether structures in the image are distinguishable from noise or not. The SNR is defined by the ratio of induced signal voltage to noise voltage. This ratio can be calculated by dividing the mean signal intensity in a region of interest (ROI) in the sample by the standard deviation of the intensity in a noise region outside the sample. The noise originates from Ohmic losses from the coil itself and its electronic components including the whole receive chain, and from the sample losses. The observed SNR strongly depends on the sensitivity of the RF coil in the target region, the magnitude of the static magnetic field, and the parameters of the pulse sequence [9,12].

2.2.8.3 g-factor and noise correlation matrix

When utilizing methods of parallel imaging, the measuring process benefits from an accelerated acquisition time as mentioned in Subsection 2.2.7.4. The enhancement is described by the acceleration factor $R > 1$ ($R = 1$ for a fully encoded image). Nevertheless, the employed undersampling leads to a reduction of the SNR in comparison to the fully sampled image. In the ideal lossless case, the SNR decreases by a factor $1/\sqrt{R}$. Furthermore, the SNR is lowered by the geometry factor g resulting from overlapping coil sensitivity profiles and correlation of the signals in an array. Thus, the relation between the SNR of the fully encoded and undersampled image is described by the following equation

$$SNR_{acc} = \frac{SNR_{full}}{g\,\sqrt{R}}\,. \qquad 2.24$$

Ideally, the sensitivity profiles of the array elements are uncorrelated across the whole imaging volume resulting in a small g-factor, close to one. Due to this spatially varying noise amplification, other approaches of calculating the signal-to-noise ratio have to be considered [10,15].

Robson *et al.* [39] presented a Monte Carlo based method called "pseudo multiple replica method". For this approach, a scan of the noise amplitude and correlation and an accelerated image acquisition is necessary to calculate the image noise. Thus, the SNR and additionally the g-factor can be acquired.

The noise correlation between the coil elements of the array can be summarized in the noise correlation matrix. It is a measure of the pairwise coupling between coil elements which leads to the undesirable induction of signal from one coil to another.

3 Methods

In this Chapter, the physical and electronical characteristics of three single element coils and two 4-channel coil arrays are described. First, the development process of the constructed coils and their interfacing circuitry is depicted as well as the used components. Then, the measurement techniques for bench tests in order to analyze and evaluate RF coils are presented. Finally, the MR experiment setup, the applied RF sequences and the subsequent data analysis for the comparison between the different coil designs is specified.

3.1 Single element coils

3.1.1 Coil construction

All three single element coils were built with a diameter of 8 cm. This corresponds to a perimeter of 25.1 cm which is why the stranded wire and the standard coil were segmented in two halves by capacitors, to remain within the limits of $\lambda/20$ to $\lambda/10$ (see Subsection 2.2.3). The diameter results in a certain penetration depth which determines the biomedical application for which it is optimized. As a rule of thumb, the penetration depth of a coil corresponds approximately to its diameter. Therefore, the built coils could be applied for example for MR imaging of the breast, head or knee. The described coils in this Subsection are all resonant near the Larmor frequency of ^{1}H nuclei (123.2 MHz for the 3T MR scanner used in this project). First, they were constructed without interfacing circuitry, as described in the following and shown in Fig. 3.1.

3.1.1.1 Stranded wire coil

The coil consisted of a flexible and non-magnetic ÖLFLEX® HEAT 260 SC (LAPP Austria, Linz) stranded wire with a diameter of 1.02 mm (1.74 mm with PTFE insulation). The cable is composed of 19 single silver-plated copper wires. The SWC was segmented by a 15 pF capacitor and on the opposite by a 14.7 pF capacitance (12 pF ‖ 2.7 pF). They are connected to the wire by soldering it onto a small printed circuit board (PCB).

3.1.1.2 Coaxial coil

The implemented flexible coaxial cable for the CC was a non-magnetic Temp-Flex 100193-5047 (Molex, Lisle, USA) with a diameter of the outer conductor of 1.17 mm (1.42 mm with FEP insulation) with a FEP dielectric. For the construction of an outer gap, the outer conductor was cut and removed over a length of 5 mm, leaving the dielectric and the inner conductor intact. For isolation and stability, a heat shrink tubing covered the gap. The inner gap also represents the coil port, where the cable is cut and only the outer conductor is soldered back together.

The self-resonance of a single-gap single-turn coaxial coil with the chosen coil geometries and cable properties is approximately at 136.8 MHz, which is close to the desired Larmor frequency of 123.2 MHz. This was calculated using MATLAB R2020a (The MathWorks, Inc., Natick, MA, USA) by approximating the coaxial coil to an ordinary conductive wire loop and applying the resonance condition.

3.1.1.3 Standard coil

For the standard coil, a copper wire with a diameter of 1 mm was used. Similar to the SWC, the coil is tuned by two capacitances: one 15 pF and one 14.7 pF capacitor (12 pF ‖ 2.7 pF). They were soldered on the coil on a conductor board, connecting the two halves of the cut wire loop. In contrast to the two coils described above, this radio frequency coil is rigid.

Fig. 3.1: Constructed stranded wire (left), coaxial (middle), and standard coil (right) without coil interface. SWC and SC are segmented in two halves by capacitors.

3.1.2 Coil interfaces

This Subsection describes the individual interfacing circuitries for each RF coil, constructed as depicted in Section 3.1, and implemented electrical components for the coil interfaces of the SWC, CC and SC. All used inductances were built by hand by winding a 0.5 mm copper wire around a plastic washer, forming a toroidal coil with the desired inductance by adapting the size and number of windings. As they are self-wound, only approximations of the values of the inductances are given. For this estimation, the resonance frequency of the inductor soldered onto a capacitor of known value forming an LC resonator, was measured on the network analyzer with a double-loop probe (see Subsection 3.4.3), allowing to calculate the inductance. 5.6 µH RF chokes were used on all interfaces for the active detuning network, blocking radio frequencies while allowing DC to pass.

3.1.2.1 Tuning, matching and active detuning

A circuit diagram of the interfaces for the stranded wire/standard coil and coaxial coil can be seen in Fig. 3.2. It includes the tuning, matching, and active detuning network but does not show the implemented Balun for the single element coils. The electrical components are labeled in this diagram and their values are summarized in Tab. 3.1. For the fine tuning of the SWC and SC a variable capacitor (also called trimmer) is connected in parallel to a fixed capacitor. A photograph of every coil with respective coil interface is shown in Fig. 3.3.

component	SC	SWC	CC
C_T	12 ‖ 3-10 pF	15 pF	-
C_{TM}	33 pF	5.6 ‖ 3-10 pF	-
C_M	56 pF	22 pF	5.6 pF
C_{AD}	12 pF	27 pF	-
L_{AD}	≈ 109 nH	≈ 48 nH	-
L_T	-	-	≈ 360 nH

Tab. 3.1: Values of the used electrical components for the interfacing circuitry of the three 1-ch coils.

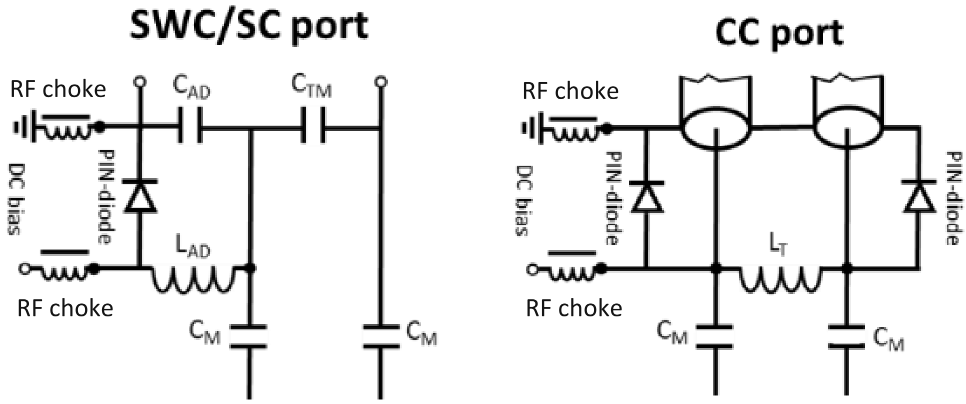

Fig. 3.2: Circuit diagram of matching, tuning, and active detuning network of the SWC/SC and the CC.

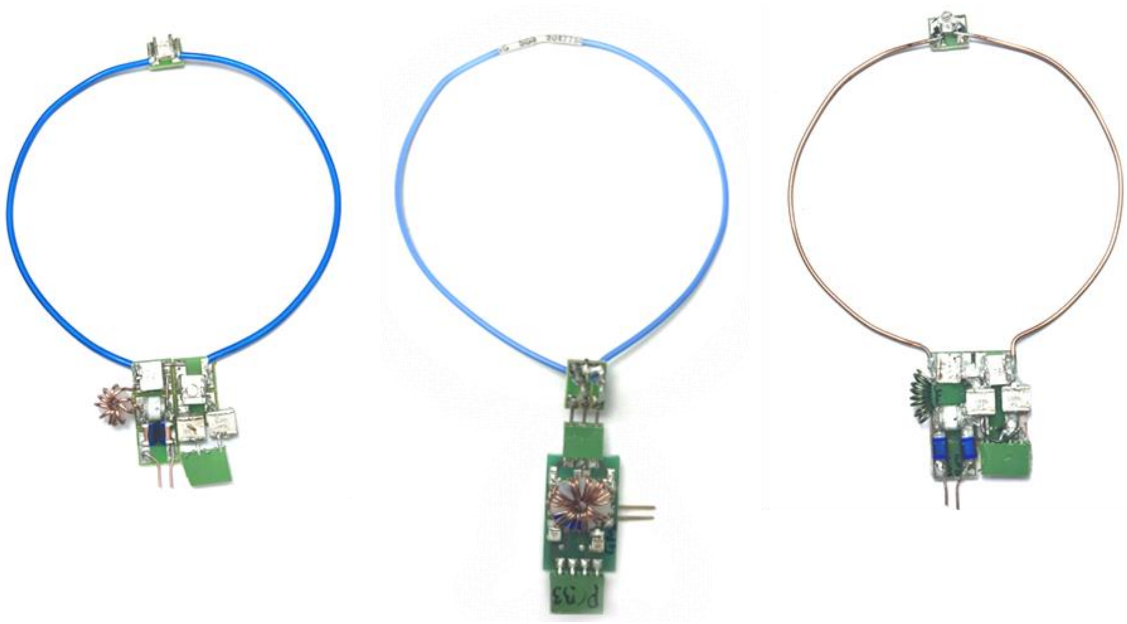

Fig. 3.3: RF coils with interfacing circuitry: SWC (left), CC (middle), and SC (right).

3.1.2.2 Balun

To connect the balanced coil to an unbalanced line, an LC-Balun (described in Section 2.2.5) was built. This electrical transformer is necessary if the signal attenuation S_{11} on the network analyzer appears asymmetrical about the resonance frequency. The balun transformer is constructed from two capacitors C_B (opposite to each other) and two inductances L_B, forming a bridge. The capacitors on this bridge had both 25.5 pF (18 pF ‖ 7.5 pF) and the self-built inductances had ~71 nH. These values were first calculated using Eq. 2.19 (results: C_B=25.8 pF and L_B=65 nH) and then further optimized to achieve a symmetric S_{11} signal. The Balun, which was used for all single element coils, can be seen in Fig. 3.4.

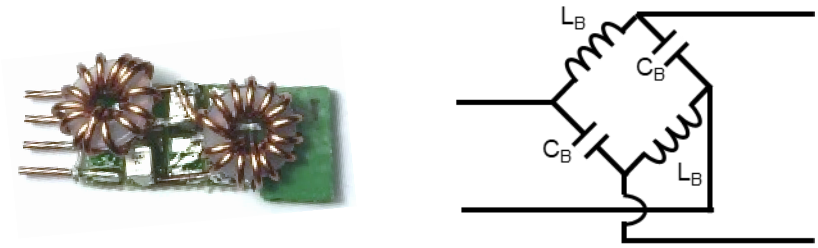

Fig. 3.4: Built LC-Balun (left) with two capacitances C_B and two toroidal inductors L_B, which is plugged in between matching network and preamplifier for the single element coils. Circuit diagram of the transformer (right).

3.2 4-channel SWC array

3.2.1 Coil construction

The stranded wire coil array consisted of four single coils which were arranged as shown in Fig. 3.5. Each element was built out of the same stranded wire as the single element coils with a loop diameter of 8 cm. The stranded wire loops were segmented twice by tuning capacitors, once at the coil port and once on the opposite side. The PCB-interface was positioned in the center of the array.

For optimal geometric decoupling, the coil centers should be distanced from each other at approximately 75 % of their diameter, which corresponds to 6 cm, as discussed in Subsection 2.2.6. The coils were positioned according to this arrangement, nevertheless the coil positions had to be slightly adapted during the bench measurements for optimal results (see Subsection 3.5.6). This can be explained by small imperfections regarding cable length, circular shape of the coils and other geometric or physical differences. Two of the coils are not overlapping and therefore were primarily decoupled by preamplifier decoupling. A photograph of the array is shown in Fig. 3.6.

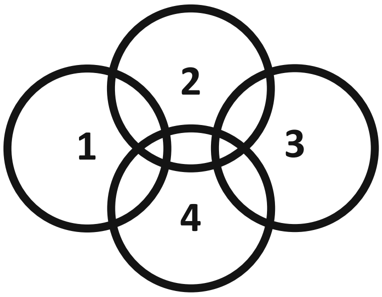

Fig. 3.5: Geometric arrangement of the four coils in the SWC array with optimal overlap for minimal coupling between the elements.

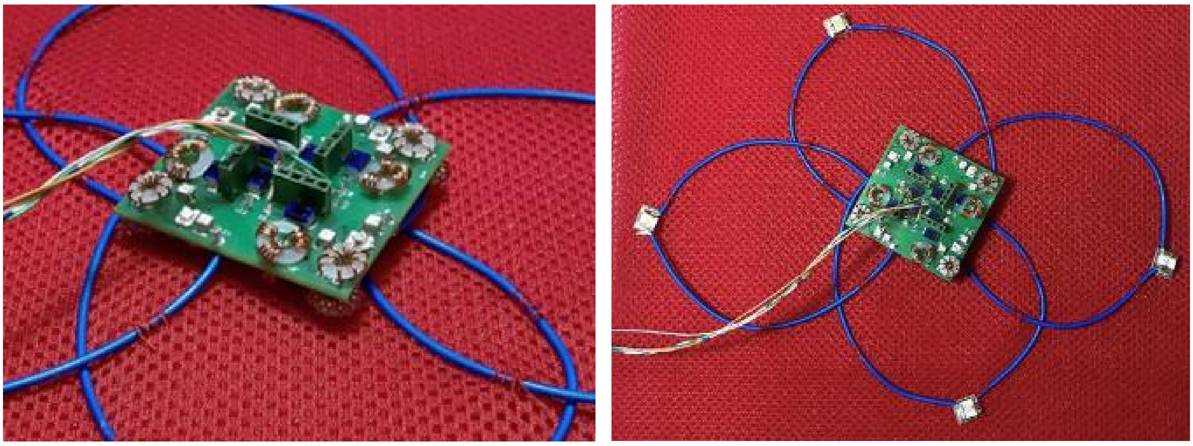

Fig. 3.6: 4-channel SWC array with PCB coil interface in the middle sewed on a fabric in the geometric arrangement depicted in Fig. 3.5 with small adaptions for minimal overlap coupling.

3.2.2 Coil interface

The coil interface for the 4-channel stranded wire array consisted of the same interface components as the single element SWC, except for the phase shifter. The circuit diagram can be seen in Fig. 3.7. Additionally, the array interface included a fuse to provide overcurrent protection in case the active detuning circuit should fail. The fuse acts as an electrical short below a certain threshold current. When exposed to higher current, the connection melts leading to an open circuit. The coil diameter of each element remained 8 cm.

3.2.2.1 Phase shifter

To adapt and optimize the impedance at the coil port seen from the RF coil to ensure preamplifier decoupling, a phase shifter was implemented into the coil interface between the Balun and the preamplifier. To achieve the desired phase shift of 90°, different electrical networks were tested such as high pass tee filter. Nevertheless, there are different approaches to create a shift in phase with lumped elements such as a high/low pass pi or low pass tee network, which are presented in Fig. 3.8. Besides, transmission lines like a coaxial cable also satisfy the requirements of a phase shift of 90°. [15,40]

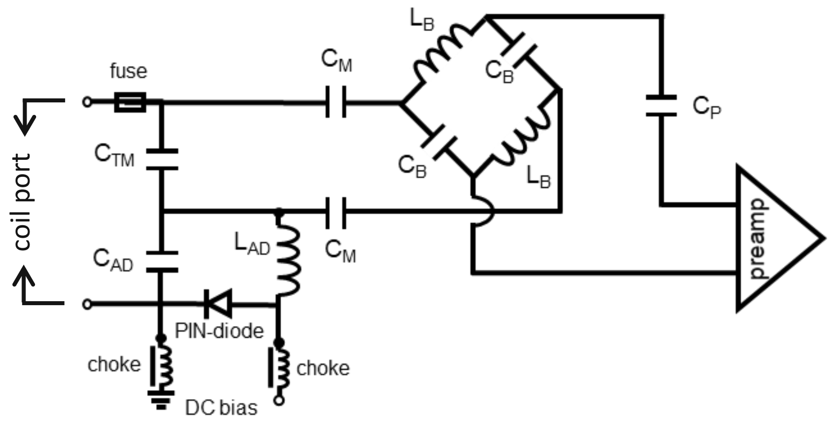

Fig. 3.7: Circuit diagram of the SWC array interface (for 1 channel) including tuning, matching, active detuning network, fuse, balun, phase shifter, and preamplifier.

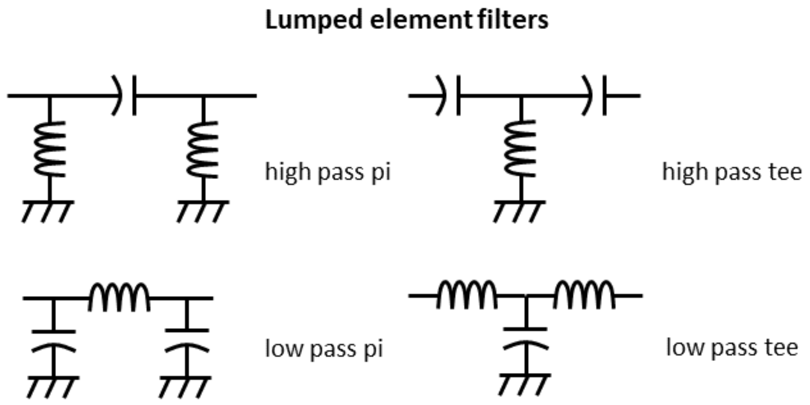

Fig. 3.8: Overview of four different lumped element filters applicable for a $\lambda/4$ phase shift [40].

However, the previous interface components also create a shift in phase, hence the phase shifter itself does not need to be at exactly 90°. Depending on the electrical components of the interface, also a single capacitor can be sufficient as a phase shifter. This was the case for the SWC, where a capacitor of 18 pF was implemented. To simplify measuring on the network analyzer, the capacitor was soldered on a pluggable solder pad, see Fig. 3.9. The optimal capacitor for sufficient preamplifier decoupling was chosen as described in Subsection 3.5.6.

Fig. 3.9: Pluggable phase shifter consisting of a single capacitor (left) and its circuit diagram (right).

3.2.2.2 PCB Design

After testing the coil interface of the SWC on the network analyzer, the necessary components for 4-channels were arranged on a single printed circuit board (PCB) to simplify and miniaturize the interface. The PCB was designed in KiCad (version 5.1.5), an open-source software suite for electronic design automation (EDA). It allows to create schematics for electronic circuits and transform it to a PCB layout. The schematic editor can be seen in Fig. 3.10, the PCB editor in Fig. 3.11, showing the specifications for the SWC array. A 3D view of the PCB from both sides is shown in Fig. 3.12.

The dimensions of the designed PCB are 46×47 mm. The track width was set to 1 mm and the minimum distance between tracks to 0.7 mm to avoid possible coupling. The pads have a HAL-coating (hot air leveling), which is a non-magnetic coating technique suited for MR-scanner compatibility. The PCB was ordered and printed via Beta LAYOUT GmbH (Aarbergen, Germany).

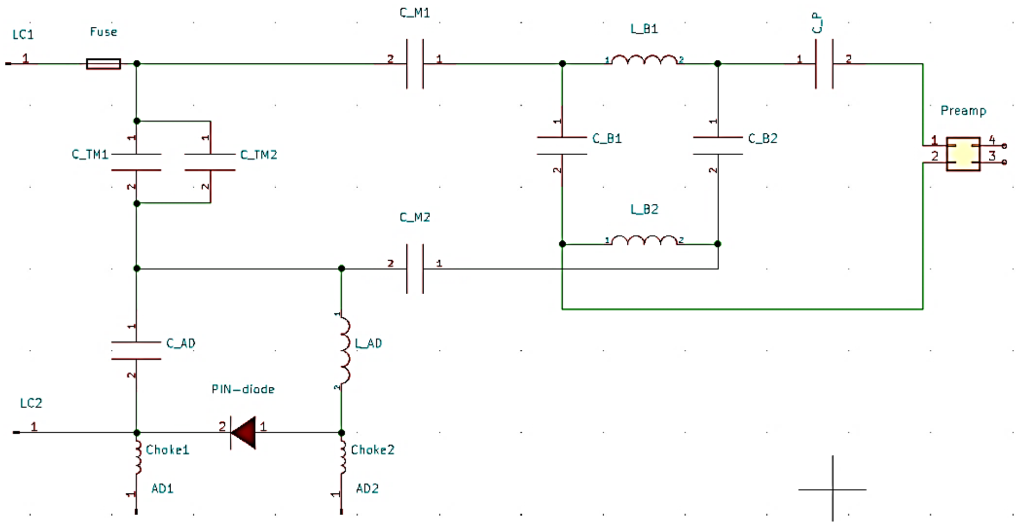

Fig. 3.10: Schematic editor in KiCad: circuit diagram of the SWC array interface (for 1 channel).

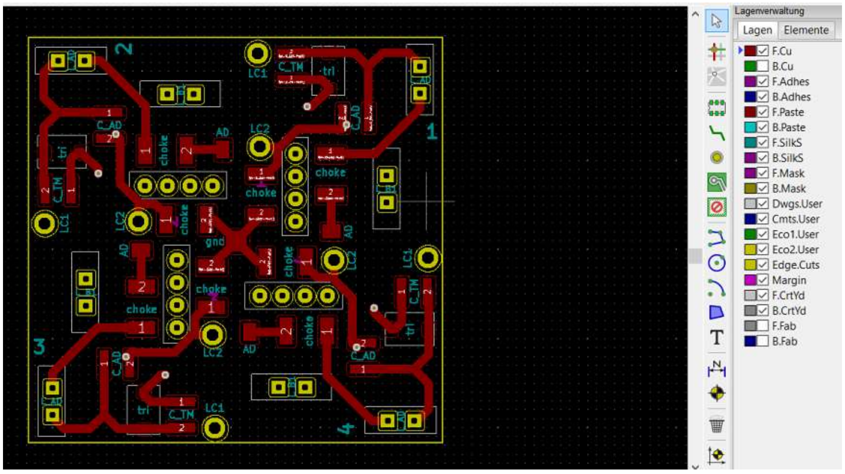

Fig. 3.11: PCB editor in KiCad: front side of the PCB of the 4-channel SWC array interface.

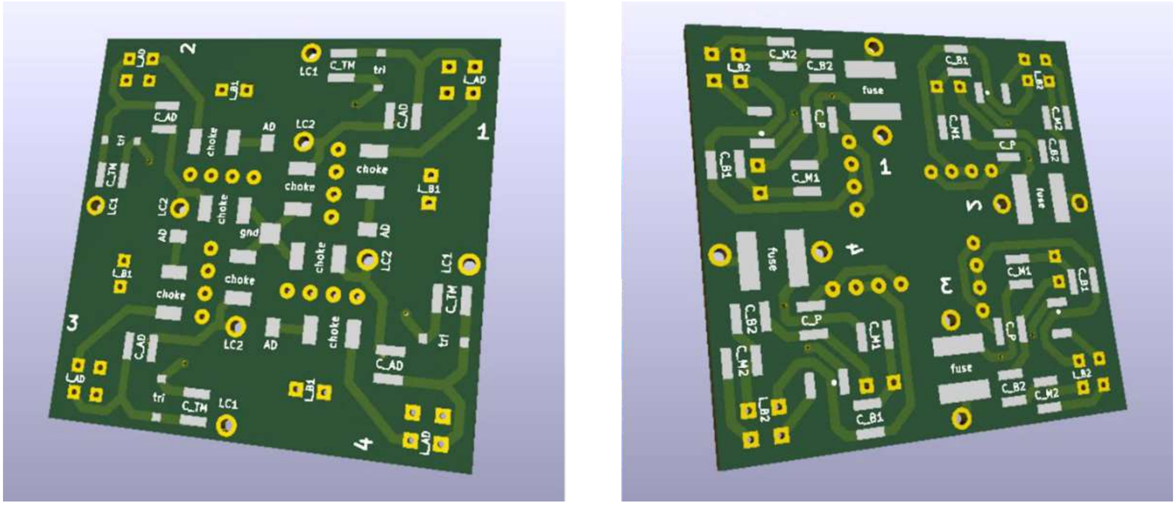

Fig. 3.12: 3D viewer in KiCad showing the 4-channel SWC PCB-interface from both sides.

3.2.2.3 Final adaptions

As the PCB interface slightly changed the resonance frequency, the tuning and active detuning network had to be adapted. C_P had to be increased which can be explained by the difference in length of the conductor paths (tracks) affecting the shift in phase. Further adaptions due to mutual influence of the coil channels included slight changes of the matching interface. The final interface components are summarized in Tab. 3.2. Furthermore, the grounds of the preamplifiers were additionally connected on the interface.

Components of SWC array

C_T	15 pF
C_{TM}	3.3/5.6/1.2/3.3 ‖ 3-10 pF
C_M	12 pF
C_{AD}	27 pF
L_{AD}	≈ 40 nH
C_B	18 ‖ 7.5 pF
L_B	≈72 nH
C_P	27 pF
RF chokes	5.6 µH

Tab. 3.2: Electrical components of the interface of the SWC array. For C_{TM}, used capacitances of each channel are listed.

3.3 4-channel CC array

3.3.1 Coil construction

The 4-channel CC receive array, shown in Fig. 3.13, was constructed from single-turn single-gap coaxial coils and had similar geometric properties as the SWC array: The single coil elements had the same size and were arranged in the same order regarding coil position. The overlap of the coils in the two arrays slightly differs as the coils were individually positioned for optimal geometric decoupling. It consisted of the same coaxial cable as the constructed single element CC described in Subsection 3.1.1.2. The diameter of the single coil elements remained 8 cm.

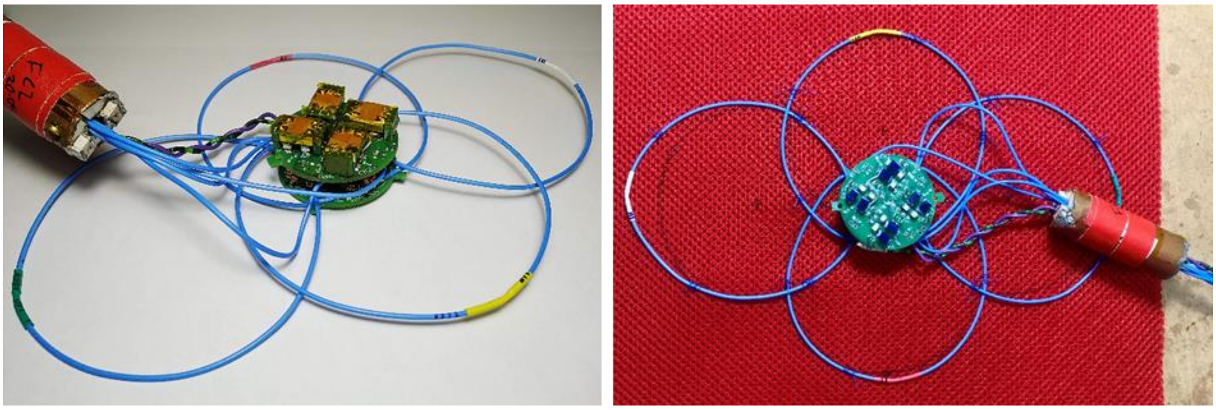

Fig. 3.13: 4-channel coaxial coil array with coil interfaces in the middle and further connection from the preamplifier on the layered PCB to the receiver chain with floating cable trap. The coil elements are sewed on a fabric with optimal overlap for minimal coupling (right).

3.3.2 Coil interface

The coaxial coil array interface has the same tuning, matching and active detuning network as the single element CC, extended by a Balun and phase shifter, which again only consists of a single capacitor. Furthermore, a fuse is placed between the outer conductors of coaxial cable at the coil port. The circuit diagram of one channel of the array is shown in Fig. 3.14 and the used electrical components are summarized in Tab. 3.3. This coil interface was miniaturized to satisfy the design constrictions of a wearable breast coil array being developed in our lab. Therefore, the interface was designed in a layered PCB and smaller preamplifiers were used.

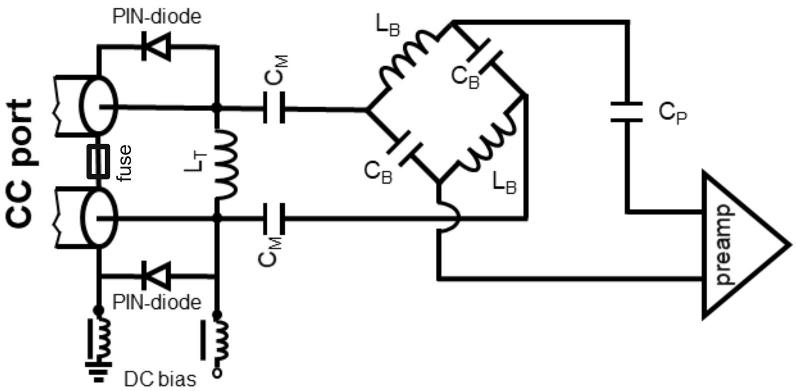

Fig. 3.14: Circuit diagram of the CC array interface (for 1 channel): fine tuning, matching network, AD, fuse, LC-Balun, phase shifter, and preamplifier.

Components of CC array

L_T	≈ 360 nH
C_M	4.7 pF
C_B	22 pF
L_B	≈ 68 nH
C_P	47 pF
RF chokes	5.6 µH

Tab. 3.3: Electrical components of the interface of the CC array.

3.4 Measurement components

3.4.1 Preamplifiers

3.4.1.1 Single element coils and SWC array

An MR-compatible low-noise preamplifier (MPB-123R20-90, HI-Q.A. Inc., Ontario, Canada) was chosen with a fixed Re(Z) of ≈ 1.4 Ω and an adjustable Im(Z) reaching from 3 Ω to 32 Ω. Both the reactance and the gain (between 25 to 32 dB) can be adapted to the desired value on the preamplifier by a small screw. The dimensions of the preamplifier are 12x20x10 mm. Photographs of the preamplifier can be seen in Fig. 3.15.

a) b)

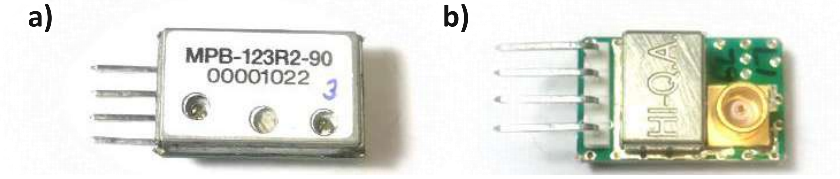

Fig. 3.15: Preamplifier used for MRI measurements: (a) front with screws for adapting reactance and gain and (b) back side.

3.4.1.2 CC array

Due to the miniaturized PCB interface, a smaller preamplifier (MSM-123281, MICROWAVE Technology Inc, Fremont, CA, USA) was used for the CC array. It has a fixed gain of 28 dB and a low input impedance (2 Ω), which is not adjustable in contrast to the other preamplifier. Its dimensions are 9×11×4 mm. A photograph of the preamplifier can be seen in Fig. 3.16. For comparison, the CC array was measured with the HI-Q.A. preamplifiers as well.

Fig. 3.16: MICROWAVE Technology MSM preamplifier used for the CC array.

3.4.2 Phantoms

The loaded measurements were performed in presence of a phantom which imitates certain properties of human tissue such as electrical conductivity. This is necessary as the characteristics of the RF coil are influenced by variations of the loading condition. One phantom consisted of a 5 liter plastic tank (24×19×14 cm) filled with a saline solution with 1.6 g NaCl/l deionized water. It had a DC conductivity of 0.2 S/m and was doped with 1 ml/l Gd. Gadolinium is used as a paramagnetic contrast agent adapting the acquisition time in MRI experiments as it shortens T_1 [41]. A second phantom was built for the bending experiments of the single element coils. It was a balloon filled with 3 liter of the same liquid, capable of adapting to the studied bending radius. The 5 liter tank phantom is shown in Fig. 3.17.

Fig. 3.17: A 5 liter tank phantom used for flat measurements of the RF coils. It is filled with saline solution doped with a Gd based contrast agent.

3.4.3 Cable traps

For MRI measurements, floating cable traps tuned to the Larmor frequency were added to eliminate induced common mode currents from the transmit coil flowing on the outer shield of the coaxial cables [42]. These shield currents can lead to the destruction of electrical components and heating in the sample, posing a potential safety issue. Floating traps have a hollow cylindrical shape and surround the coaxial cables where shield currents should be blocked. They consist of a dielectric (here: PTFE) which is cut in two halves and covered with a layer of copper on the inner and outer surface. One end is shorted and on other end is connected by a capacitor, tuning the trap to the desired frequency. Fine tuning is accomplished by adapting the distance between the two half-cylinders. This is realized by four screws functioning as a spacer working against the pressure of a tightly adjusted cable tie. Fig. 3.18 shows the structure of a floating cable trap, the self-built version can be seen in Fig. 3.19.

Fig. 3.18: Schema of a floating cable trap: hollow cylinder (cut in half) which is covered with copper foil and tuned by capacitors placed on top of each half.

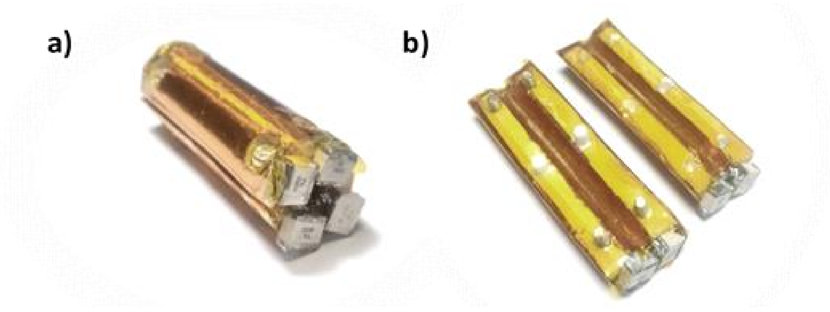

Fig. 3.19: Self-built floating cable trap: closed (a) and open (b). The cable trap is fine tuned by four screws which determine the distance between the two halves.

3.4.3.1 Measurement setup

The resonance frequency of the floating cable traps can be measured by a S_{21} measurement on the network analyzer [43]. For this purpose, two coaxial cables, each surrounding a ferrite choke, are connected to the ports of the network analyzer. The coaxial cables have an outer gap on the loop around the ferrite choke. Another coaxial cable is put through these chokes allowing for magnetic coupling. The measurements setup is shown in Fig. 3.20. The floating cable trap is then placed around the coaxial cable between the two ferrite chokes. This enables measuring the resonance of the trap and finetuning to the Larmor frequency by adjusting the screws.

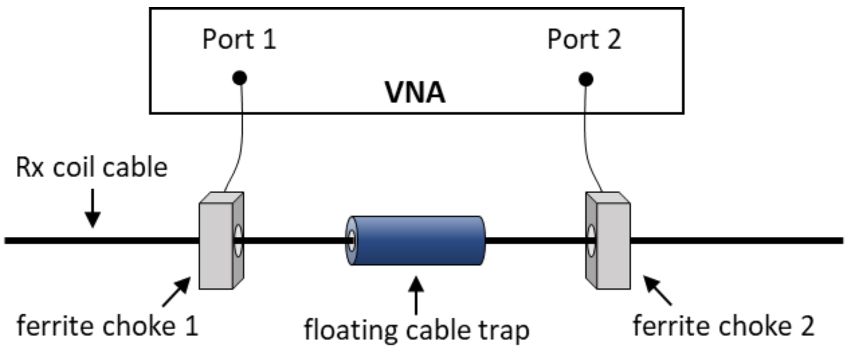

Fig. 3.20: Measurement setup of a floating cable trap: The trap is placed on the receive cable of the coil between two ferrite chokes. These chokes are the inductive link to the coaxial cables connected to the ports of the network analyzer.

3.5 Bench measurements

3.5.1 Vector network analyzer

The characteristic parameters of the coil (*e.g.*, Q-factor, resonance frequency) were measured on a vector network analyzer (VNA). It detects transmitted and/or reflected electrical wave signals of an electric network. This enables the measurement of the scattering (S-) parameters, see next Subsection. A network analyzer (E5071C, Keysight Technologies, USA) with Configurable Multiport Test Set (E5092A, KEYSIGHT Technologies, USA) was used. For all bench measurements, the S-parameters (in dB) were investigated in a signal attenuation diagram (logarithmic magnitude format) over a certain frequency range.

3.5.2 S-parameters

The scattering parameters or S-parameters are a measure for the electrical behavior of a network when exposed to wave signals. They are frequency dependent and provide information on the amplitude and phase of the transmitted or reflected signals. S-parameters are determined by the ratio of input and output signals at the ports of the network analyzer [44]. For the evaluation of the RF coil performance, experiments on the network analyzer can be realized by one or two port measurements. These represent the S_{11} and the S_{21} measurement. The two-port network and its input and output signals are pictured in Fig. 3.21.

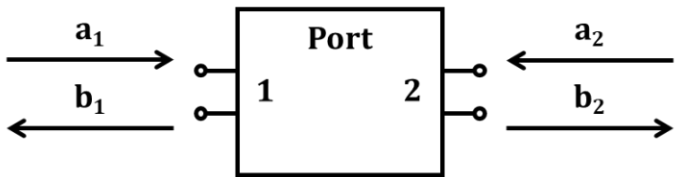

Fig. 3.21: Two-port network with input signals (a1 and a2) and output signals (b1 and b2).

The S-parameters can be displayed in form of a matrix, describing the relations between in- and output signals (voltage) for a two-port network [44],

$$\begin{pmatrix} b_1 \\ b_2 \end{pmatrix} = \begin{pmatrix} S_{11} & S_{12} \\ S_{21} & S_{22} \end{pmatrix} \begin{pmatrix} a_1 \\ a_2 \end{pmatrix}. \qquad 3.1$$

From this, the relevant scattering parameters for the following experiments can be derived

$$S_{11} = \frac{b_1}{a_1}, \qquad S_{21} = \frac{b_2}{a_1}. \qquad 3.2$$

The magnitude of the S-parameter is commonly displayed on the vector network analyzer in logarithmic scale, determining the return loss in dB,

$$S\,[\mathrm{dB}] = -10 \log |S|^2 = -20 \log |S|, \qquad 3.3$$

$$S\,[\mathrm{dB}] = -10 \log |P|,$$

with the ratio of incident to reflected power P [42].

S_{11} measurement

For measuring the resonance frequency or the Q-factor, the coil can either be directly connected to one port of the network analyzer or inductively coupled to a pickup coil. This can be a single or double pickup coil. If an RF coil is connected to one port of the analyzer via the built coil interface, the reflected signal S_{11} is picked up. In contrast to measuring with the pickup coil, this additionally gives information on the impedance matching level as the coil interface determines the reflection coefficient. The matching level of the RF coil corresponds to the S_{11}-parameter at the resonance frequency on the network analyzer.

S_{21} measurement

In the following experiments, the pickup coil was represented by a double-loop probe [45], which consists of two small coils which are geometrically decoupled. The overlap can be adapted by a screw shifting one of the coils over the other and therefore changing the geometric decoupling. It is adjusted to a S_{21} value of below -80 dB to ensure that the measured signal is not directly induced from coil 1 into coil 2, but over the device under test. This self-built probe can be seen in Fig. 3.22. The probe is connected to the network analyzer via two ports. One of these is responsible for sending a signal to the first coil which couples with the RF coil which is placed near the probe. The induced current forces the RF coil to resonate which likewise induces a signal in the second coil of the probe which can be detected by the network analyzer. This method represents measuring the S_{21} parameter which can also be applied when testing the RF coil without a coil interface.

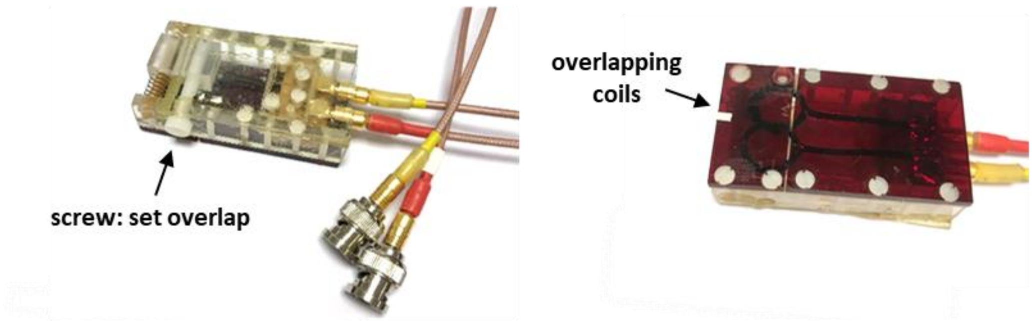

Fig. 3.22: Double-loop probe to measure the S_{21}-parameter on the network analyzer, consisting of two overlapping coils. The geometric decoupling depends on the coil overlap which is controlled by a screw.

3.5.3 Tuning and matching

The matching of the RF coil to 50 Ω at the resonance frequency is tested by a S_{11} measurement. It is important that every interface component is connected to the network analyzer (also the Balun or phase shifter) as each electrical component can influence the matching level. The properties of the phantom have an impact on it as well. To maximize the signal received by the RF coil, a high matching level, corresponding to a high percentage of transmitted power and little reflected power, is desirable. 95 % of the signal is already transmitted at -13 dB, 97 % at -15 dB. Therefore, a S_{11} parameter of about -14 dB or lower at f_0 is an appropriate guide value to minimize reflection losses sufficiently.

Furthermore, the Q-factor can be determined during this measurement. It can also be represented by the ratio of the resonance frequency to the resonance bandwidth [42],

$$Q = \frac{f_0}{\Delta f_0}. \tag{3.4}$$

The vector network analyzer uses the bandwidth of the response curve at -3 dB as Δf_0 for the calculation of this ratio. The S_{11} measurement on the network analyzer for the estimation of the tuning, matching level and Q-factor is shown in Fig. 3.23 in form of a logarithmic signal attenuation diagram.

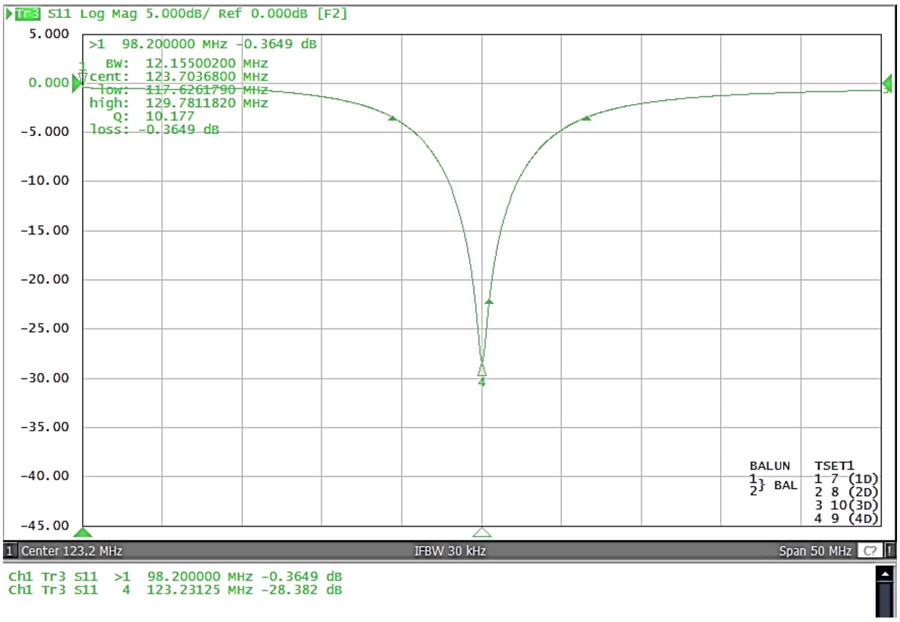

Fig. 3.23: S_{11} measurement [dB] of the resonance frequency, matching level and Q-factor on the network analyzer: The RF coil is resonant at 123.2 MHz and sufficiently matched to 50 Ω. The frequency span around 123.2 MHz was set to 50 MHz.

3.5.4 Coil noise

When measuring the unloaded Q-factor, the coil resistance R_C can be estimated as described in Subsection 2.2.8.1. It was calculated from the unloaded bench measurements by the following equation

$$R_C = \frac{L\omega'}{Q}\sqrt{\frac{\omega_0}{\omega'}}. \tag{3.1}$$

with the coil inductance L, the measured resonance frequency ω' of the coil and the desired resonance frequency ω_0 of 123.2 MHz. For comparison, the resistance of each coil was extrapolated to ω_0. It can be seen, that the resistance rises with the square root of the frequency as a consequence of the skin effect. The inductance of the coils was calculated by the resonance condition. Here, the CC was approximated to a conductive wire loop.

3.5.5 Active detuning

The active detuning was tested by a S_{21} measurement with the double pick-up coil, which is shown in Fig. 3.24. The RF coil was placed on the phantom with the double-loop probe on top of it with a distance of a few centimeters between them. The AD circuit was connected via the DC cable to a power source. The network analyzer showed the frequency peak at 123.2 MHz. When the AD circuit is activated by the PIN diode, this peak splits into two, detuning the RF coil. For ideal active detuning, the minimum between the two peaks should be at 123.2 MHz, indicating that both the RF coil and the AD circuit resonate at the same frequency. The active detuning network of all coaxial coils destroyed the resonance completely, hence no peaks at all were observed (see Fig. 3.25). To quantify the performance of the active detuning network, the difference in S_{21} between tuned and detuned state at the Larmor frequency ΔS_{21} is measured.

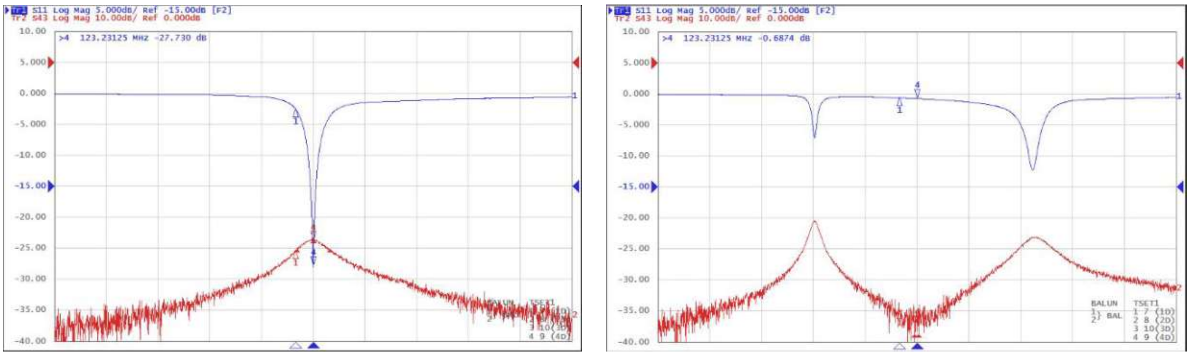

Fig. 3.24: S_{11} (blue) and S_{21} (red) measurement [dB] of the active detuning circuit on the network analyzer: tuned (left) and detuned with frequency split (right) for the SWC and SC. Note that the red curves are on a different scale (the base line of the red curve was at approximately -80 dB). A frequency span of 150 MHz around 123.2 MHz is shown.

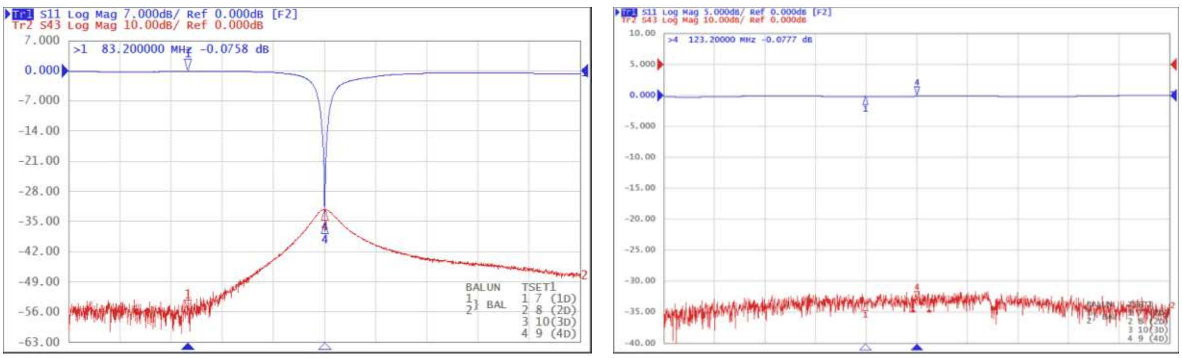

Fig. 3.25: S_{11} (blue) and S_{21} (red) measurement [dB] of the active detuning circuit on the network analyzer: tuned (left) and detuned state (right) for the CC, where no resonances occur. Note that the red curves are on a different dB scale (the red curve was at approximately -80 dB). A frequency span of 150 MHz around 123.2 MHz is shown.

3.5.6 Decoupling

3.5.6.1 Geometric decoupling

To minimize the coupling between the elements, the optimal overlap had to be adjusted for each coil pair. In order to measure the inductive coupling between the coil elements of an array, the S_{ij} parameter of each coil pair is determined by the network analyzer (i,j corresponding to a specific coil channel). Fig. 3.26 shows the measurement of the coupling signal on the network analyzer between each channel.

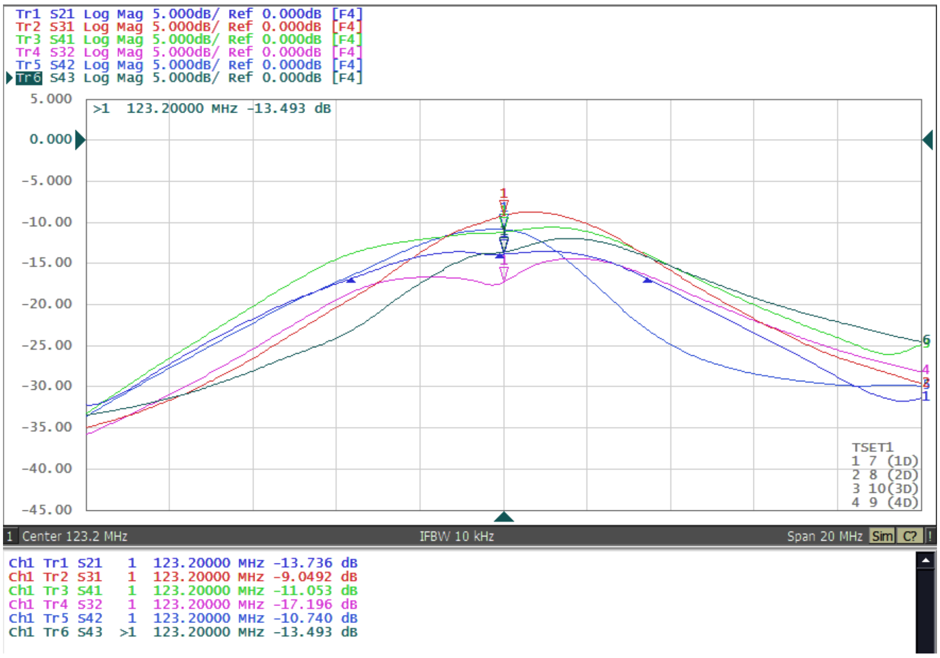

Fig. 3.26: Measurement of the S_{ij}-parameter [dB] on the network analyzer determining the inter-element coupling between the coils of the 4-channel SWC array. A span of 20 MHz around 123.2 MHz is shown.

3.5.6.2 Preamplifier decoupling

To adjust and optimize the preamplifier decoupling, a S_{21} measurement with the double-loop probe is performed. The coil is placed on the flat phantom and connected to the preamplifier, which is powered by a 10 V source. The specifications of the preamplifiers can be read in Subsection 3.4.1. When the pick-up coil is now placed above the coil, peak splitting can be observed as shown in Fig. 3.27. If the coil is decoupled, the minimum between the two peaks appears at f_0. This can be adapted by the adjustable reactance of the preamplifier or changing the electrical components of the phase shifter (adapting the capacitance). For this measurement, the other coils of the array must be connected to a 50 Ω termination. The absolute difference between the S_{21} parameter when connected to the powered preamplifier versus 50 Ω termination should be as high as possible for sufficient decoupling. Both configurations are shown on the network analyzer in Fig. 3.27.

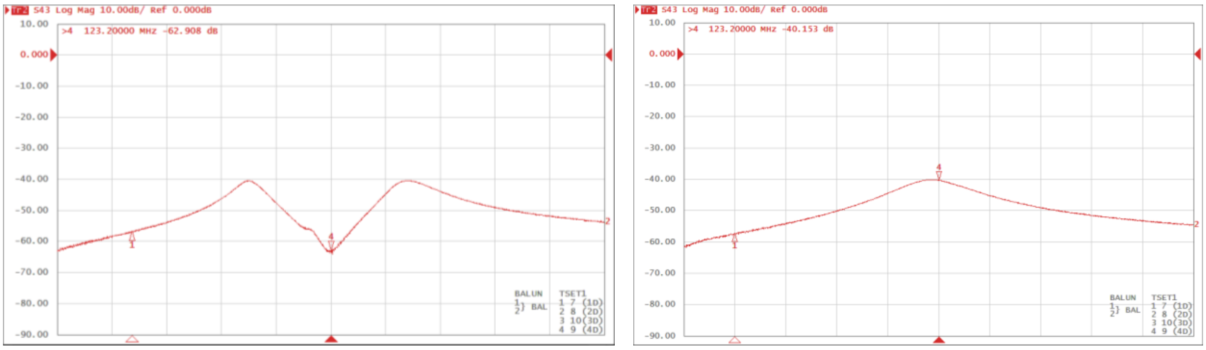

Fig. 3.27: S_{21} measurement [dB] of the preamplifier decoupling on the network analyzer with a double-loop probe: peak splitting occurring with powered preamplifier (left) and single resonance frequency peak of the coil connected to a 50 Ω termination (right). A frequency span of 40 MHz around 123.2 MHz is shown.

3.5.7 Experimental setup for single element coils

3.5.7.1 Flat and bent configuration without interface

In order to compare the coil performance (without interface, except tuning network for the SWC and SC) of the different design types upon bending, certain parameters were measured via the double-loop probe. These included the shift in their resonance frequency f_0, Q-factor and S_{21} parameter. The coils were once measured in flat configuration and once bent to a radius of 6.4 cm, both with and without a sample. For the flat measurements, the 5 liter tank phantom was used. The bent configuration was realized by putting the coil underneath a bent PTFE sheet which was fixed by a 3D printed holder setup. For the loaded measurements, the balloon phantom was placed on top of the sheet, which is shown in Fig. 3.28.

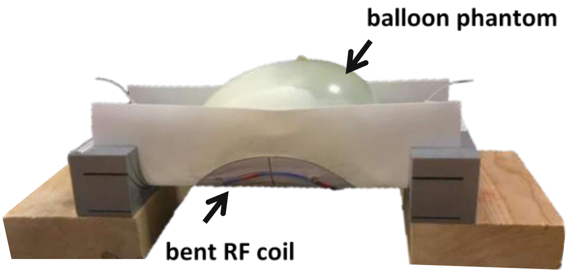

Fig. 3.28: Holder setup, in which the bent PTFE sheet is placed, with the balloon phantom on top and the RF coil underneath.

3.5.7.2 Flat configuration

The three coil types were measured on the bench with interfacing circuitry in flat configuration. The interface did not include a phase shifter as these coils were not implemented in an array, hence no decoupling from other RF coils was required. The interface was implemented in modules and the parts could be connected individually. For optimal comparison, the same LC-Balun was used for all coils. The measurements were performed with the 5 liter phantom, with the RF coil directly fixed on the tank (see Fig. 3.29). The coil was tuned and matched to this sample thus no unloaded measurements were performed. The Q-

factor and the matching level at f_0 were determined by a S_{11} measurement on the vector network analyzer.

Fig. 3.29: SWC fixed on the tank phantom for the flat measurements.

3.5.7.3 Bent configuration

The performance of the three single element coils in bent configuration with interface was tested with the balloon phantom. The experimental setup remained the same as for the coils without interface in bent configuration, except for the SC which was not fitted to the phantom. The SC was put underneath the phantom in flat configuration as the copper wire would have to be bent permanently. This is not realizable for applications that repeatedly need adaption to the shape of the phantom or body as the rigid coil could break after a few times. These two configurations are pictured in Fig. 3.30. The coils which were used for the flat measurements had to be retuned for the new setup. Only the matching network of the SC had to be adapted (C_M = 18 pF). By a S_{11} measurement on the network analyzer, Q-factors and matching levels at f_0 were determined.

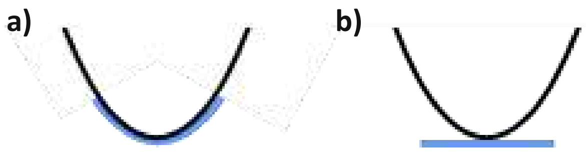

Fig. 3.30: Coil underneath the bent phantom form fitted to the shape like the SWC and CC (a) and fixed to the center in flat configuration for rigid coils as the SC (b).

3.5.8 Experimental setup for coil arrays

The 4-channel coil arrays were placed flat on the 5 liter tank phantom as shown in Fig. 3.31. For clinical applications, the coils and the electronic components must be concealed for safety reasons and to improve the robustness, resulting in a distance between coil and sample. Therefore, a fabric was placed in between coil and sample, resulting in a distance of 3 mm. The matching level at f_0 and the Q-factor were determined by a S_{11} measurement on the network analyzer as shown in Fig. 3.32.

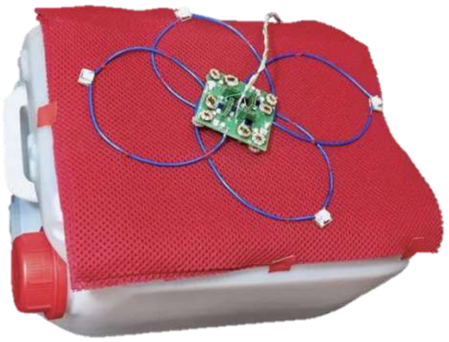

Fig. 3.31: SWC array fixed on the tank phantom with two layers of fabric in between.

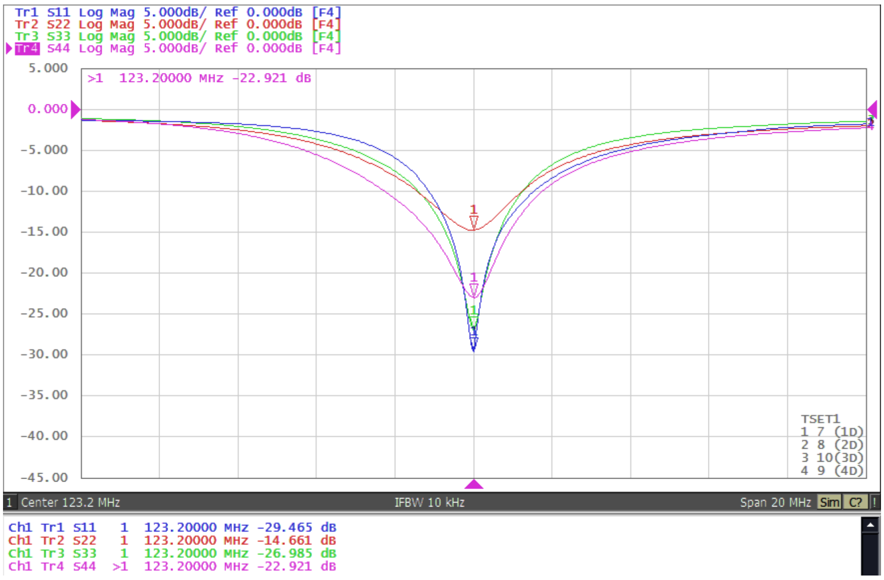

Fig. 3.32: S_{11} measurement [dB] of the SWC on the network analyzer to determine the matching level and the Q-factor for each coil channel of the array. The span of 20 MHz around 123.2 MHz is set.

3.6 MRI measurements

The magnetic resonance experiments were carried out on a 3 Tesla MR scanner (MAGNETOM PRISMA FIT, Siemens Healthineers, Erlangen, Germany). The Larmor frequency of ^{1}H nuclei on this scanner model is 123.2 MHz. The MR measurement data was analyzed using MATLAB R2020a (The MathWorks, Inc., Natick, MA, USA).

3.6.1 Single element coils

3.6.1.1 Setup

Flat configuration

The three single loop coils were tested in flat configuration on the 5 liter tank and were directly fixed on the phantom. The same coil interfaces as for the bench measurements were used to connect the SWC, CC and SC to the preamplifier. The orientation of the preamplifiers with respect to the scanner bore had to be considered as the functioning of the MosFET is dependent of its angle to the static magnetic field.

An 8-channel receive plug (see Fig. 3.33) connected to a connector board was used to plug the respective RF coil to the receive channel via a coaxial cable and the PIN diode bias lines via a twisted wire pair, see Fig. 3.34. On this connection and on the cable of the receive plug, floating cable traps are placed.

Fig. 3.33: 8-channel receive plug with floating cable traps for 3 T.

Fig. 3.34: Pluggable connector from the preamplifier to the receive plug and DC cable surrounded by a floating cable trap.

For the measurements of a transversal slice through the center of the coil, the following scan parameters were set for a 2D gradient echo (GRE) sequence: repetition time/echo time (TR/TE) = 50/10 ms, FOV = 290×290 mm^2, 0.6×0.6 mm^2 resolution, slice thickness = 6.5 mm. From this GRE sequence, the SNR was calculated as described below.

Flip angle (B_1) maps were acquired by scanning with the transmit coil only (body coil of the scanner), once with and once without the RF coil present. The second scan is used as a reference scan to calculate the change in the transmission field when the (detuned) Rx coil is present. This is necessary for the evaluation of the efficiency of the active detuning of the RF coil and thereby the decoupling from the body coil.

Bent configuration

For the bent MRI measurements, the three RF coil types were measured on the balloon phantom. The SWC and CC were adapted to the shape of the balloon, while the SC was in flat configuration. The setup of the bent configuration is described in detail in Subsection 3.5.7.3. The MRI sequence parameters were identical to the flat measurements.

3.6.1.2 MR data analysis

SNR

For the evaluation of the performance of the single loop coils, their SNR images were calculated. For this purpose, the acquired k-space data was Fourier transformed and the square root of the sum of the squares was computed. Next, a region in the image was defined which only contained noise. The ratio between image and standard deviation in the noise region results in the SNR image. The average SNR was calculated in a circular region of interest (ROI) with a radius of 1 cm placed centrally with a distance of 1.5 cm from coil to circle center for comparison of the receive sensitivities of the different coil types. Additionally, the relative SNR between coil types was calculated. For the measurements in bent configuration, the ROI had a radius of 1 cm and the center of the ROI was located 2 cm from the coil center on top of the phantom.

B_1 distortion

The active detuning circuitry was evaluated by dividing the measured B_1 maps (with the RF coil present) by the B_1 reference scan (without coil). This allows to plot the distortion of B_1 caused by the RF coils. Due to slight inevitable changes of the alignment of the respective phantom between measuring the B_1 maps as well as partial volume effects, inaccuracies can occur in the calculation, particularly at object borders. A Gaussian filter was applied to reduce the effect of image noise on the evaluation. Furthermore, a mask based on the image magnitude was applied to suppress the air background outside the phantom.

3.6.2 4-channel coils

3.6.2.1 Setup

For the flat measurements, the 5 liter tank phantom was used. Two layers of fabric were placed on the phantom to keep a distance of about 3 mm between sample and coil. On top, the SWC and CC array was fixed. Analogously to the single element experiments, the four preamplifiers of the array were connected to the 8-channel receive plug by coaxial cables shielded by a floating cable trap. The setup can be seen in Fig. 3.35. The CC array was tested with the HI-Q.A. preamplfiers as well, to compare them to the MwT preamplifiers.

The imaging parameters were set as follows for the 2D GRE sequences for all orientations: The TR/TE was 470/3.23 ms. The resolution was 1.0×1.0 mm^2 and the slice thickness 3 mm with a distance factor of 0 %. The orientation-specific parameters are depicted in Tab. 3.4.

The B_1 maps for both arrays were acquired as described in the prior Section for the single element coils. A noise-only scan was performed for the calculation of the noise correlation matrix. For this purpose, a scan without prior excitation pulse was acquired.

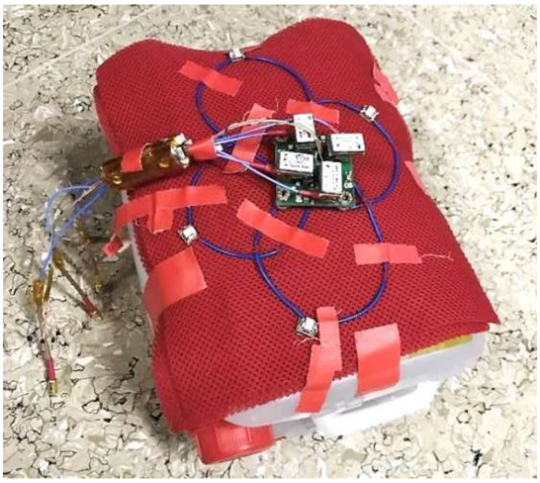

Fig. 3.35: SWC fixed on textile on the tank phantom. The array is connected to preamplifiers with Rx cables which are shielded by a floating cable trap. The CC array was fixed similarly.

orientation	FOV [mm^2]	nr. of slices
transversal	224 x 200	60
sagittal	288 x 232	52
coronal	288 x 288	20

Tab. 3.4: Orientation-specific imaging parameters of the 2D GRE sequences: Field of view and number of slices.

3.6.2.2 MR data analysis

SNR and noise correlation matrix

For the comparative study of the two coil arrays, their SNR images were calculated. For this purpose, the pseudo multiple replica method was applied [39]. Using the data of the noise-only scans of each coil channel the 4×4 noise correlation matrix is determined. Random noise was generated and correlated by this matrix. This noise was added to the k-space data prior to image reconstruction. The procedure was repeated for 256 replicas of each accelerated image. The image reconstruction consists of the following steps: First, each replica was Fourier transformed. Then, to combine the images of the four channels, the square root of the sum of the squares of the images of each coil element is calculated. This method, as described by Roemer *et al.* [18], results in high SNR in comparison to other combination techniques. The SNR is given by dividing the mean of each pixel over the number of replicas by the respective standard deviation.

A three-dimensional ROI beneath the coil arrays was defined for the coronal orientation to compare the SNR. This ROI was set to a cylinder with a base diameter of 16 cm and a height of 5.1 cm, which corresponds to 17 slices. The circular base is parallel to the plane of the coil array and starts approximately 1 cm beneath the surface of the phantom.

g-factor

The g-factor is calculated using Eq. 2.24. For this purpose, images with acceleration factors of R = 2 were simulated by skipping k-space data points (only half of the data is used for R = 2, with R = 1 representing the image without acceleration). This corresponds to the number of coils in phase encoding direction, which is from right to left for the coronal slices. Thereby, fully sampled and undersampled images were generated, enabling the calculation of the g-factor.

B_1 distortion

From the measured flip angle maps, the B_1 distortion was calculated by dividing the scan with RF coil present by the reference scan. Similar as for the single element coils, a gaussian filter and a mask, surrounding the phantom, were applied.

4 Results

This Chapter presents the results of bench tests and MR measurements which were performed with the constructed RF coils. It gives a comparison between the presented single loop coil designs as well as 4-channel coil designs with respect to their robustness to bending, Q-factor, matching level, inter-element decoupling, SNR, g-factor, and active detuning.

4.1 Single element coil comparison

4.1.1 Bench measurements

4.1.1.1 Flat and bent configuration without interface

The coil performance upon bending was measured as described in Subsection 3.5.7.1 and the results are summarized in Tab. 4.1. The resonance frequency only increased slightly when bending the coil as the deviation remained under 1 % for the unloaded measurement and between 1.3 % and 2.7 % for the loaded one. The shift of f_0 is presented in Fig. 4.1. This indicates robustness upon bending for all coil types in terms of matching, even though the rigid wire of the SC was permanently bent. Significantly lower unloaded Q-factors and consequently lower Q-ratios were observed for the CC. The change of the Q-factor was not consistent, it decreased for the SWC and SC but rose minimally for the CC when measuring without a sample. In presence of a sample the change of the Q-factor was between 73 % and 86 % which can be explained partly by the different phantom sizes. For the bent measurement, the balloon phantom only had 3 liter instead of 5 liter resulting in weaker loading by the sample. All Q-ratios were above 5.5 indicating sample noise dominance, which is shown in Tab. 4.2. S_{21} parameters were sufficiently low for all measurements (-40 to -38 dB) implying that the presence of the double loop-probe did not influence the result.

		flat		bent		flat vs. bent	
	coil type	**f_0 [MHz]**	**Q**	**f_0 [MHz]**	**Q**	**f_0 shift [%]**	**Q change [%]**
unloaded	SC	123.6	437	124.8	419	0.97	-4.12
	SWC	123.5	473	124.6	443	0.89	-6.34
	CC	131.1	181	132.1	182	0.76	0.55
loaded	SC	121.0	22	122.6	39	1.32	77.27
	SWC	121.0	21	122.6	39	1.32	85.71
	CC	124.4	19	127.7	33	2.65	73.68

Tab. 4.1: Results of the bending performance comparison: unloaded and loaded measurements of the three coil types: resonance frequency f_0 and Q-factor in both configurations and their deviation due to bending.

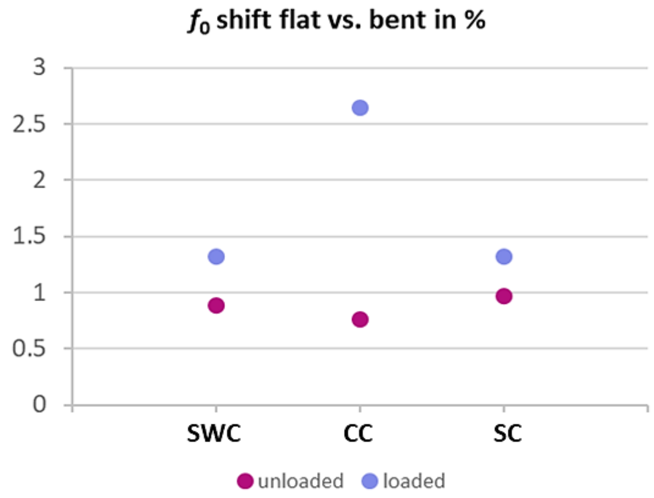

Fig. 4.1: Shift of the resonance frequency due to bending in comparison to the flat measurement with and without a sample (loaded and unloaded).

coil type	Q-ratio: flat	Q-ratio: bent
SC	19.9	10.7
SWC	22.5	11.4
CC	9.5	5.5

Tab. 4.2: Q-ratios of the SWC, CC, and SC in flat and bent configuration.

The results of the calculation of the coil noise from the unloaded measurements in flat configuration are shown in Tab. 4.3. It shows that the coil resistance of the CC is significantly higher than for the SC and SWC. As expected, the inductance of the coils was very similar.

coil type	R_C [mΩ]	L [nH]
SC	396.2	223.3
SWC	366.5	223.7
CC	954.5	216.4

Tab. 4.3: Coil resistance R_C and coil inductance L of the three coil types.

4.1.1.2 Flat configuration

The characteristics of the RF coil and its respective interface were determined on the bench as depicted in Subsection 3.5.7.2. The results are listed in Tab. 4.4 and show the loaded Q-factor, matching level S_{11} and the difference ΔS_{21} between tuned and detuned state. The Q-factors did not decrease in comparison to the measurements without coil interface indicating no rise in coil noise introduced by the interfacing circuitry. The S_{11}-parameters were sufficiently low, indicating good matching of the coil impedance to 50 Ω. The ΔS_{21} values show the effective operation of the active detuning network.

coil type	Q-factor	S_{11} [dB]	ΔS_{21} [dB]
SC	20	-26.3	27.8
SWC	22	-39.8	27.1
CC	35	-24.9	28.5

Tab. 4.4: Bench measurement of the coils with interface in flat configuration. Q-factor, matching level (S_{11}-parameter) and ΔS_{21} at 123.2 MHz are shown.

4.1.1.3 Bent configuration

The results of the measurements of the three single element coils in bent configuration, performed as described in Subsection 3.5.7.3, are summarized in Tab. 4.5. Higher Q-factors and S_{11}-parameters were observed when compared to the flat measurements. This is due to the bending of the coils and the different phantom sizes influencing the matching level.

coil type	Q-factor	S_{11} [dB]
SC	42	-28.5
SWC	27	-18.2
CC	41	-18.7

Tab. 4.5: Bench measurement of the single element coils with interface in bent configuration. Q-factor and matching level at 123.2 MHz are shown.

4.1.2 MRI experiments

4.1.2.1 Flat configuration

SNR

The MR measurements of the three single loop RF coils on a flat phantom in the 3 T scanner were performed as depicted in Subsection 3.6.1.1. Their calculated SNR maps can be seen in Fig. 4.2., where the defined circular ROI is drawn. The signal-to-noise ratio in this region, which is shown in Tab. 4.6, was between 510 and 570 for all coils with the highest value from the SC as expected. Compared to this coil, the SNR loss of the SWC in this region was 3.8 % and 9.4 % for the CC. Even though the SWC and CC designs do not show a sensitivity gain in flat configuration, the SNR loss is rather small, and it should be considered, that these coils are designed to provide higher signal when they are bent and adapted to the shape of a sample.

coil type	SNR	vs. SC [%]
SC	543	-
SWC	543	-3.8
CC	511	-9.4

Tab. 4.6: Signal-to-noise ratio of the three measured RF coils in the ROI and the relative SNR loss when compared to the standard coil.

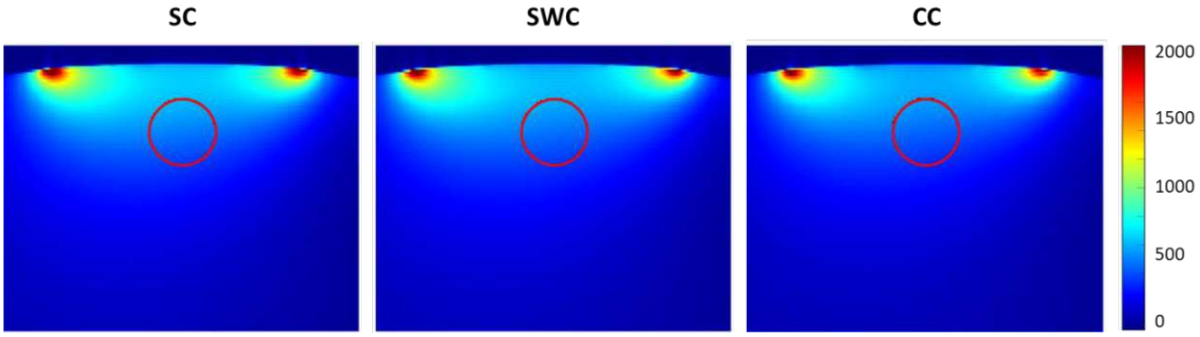

Fig. 4.2: SNR maps calculated from GRE of a transversal slice of the SC, SWC, and CC. The images are cropped, and the red circle depicts the defined region of interest.

B_1 distortion

The B_1 distortion maps illustrating residual coupling between the RF and body coil can be seen in Fig. 4.3. The active detuning circuitry of the CC showed better performance than the one of the SC and SWC. Nevertheless, the results indicate sufficient decoupling from all examined RF coils to the transmit coil as the mean B_1 change over the whole phantom stayed within ± 19 %. The minimal and maximal B_1 change for each coil can be seen in Tab. 4.7.

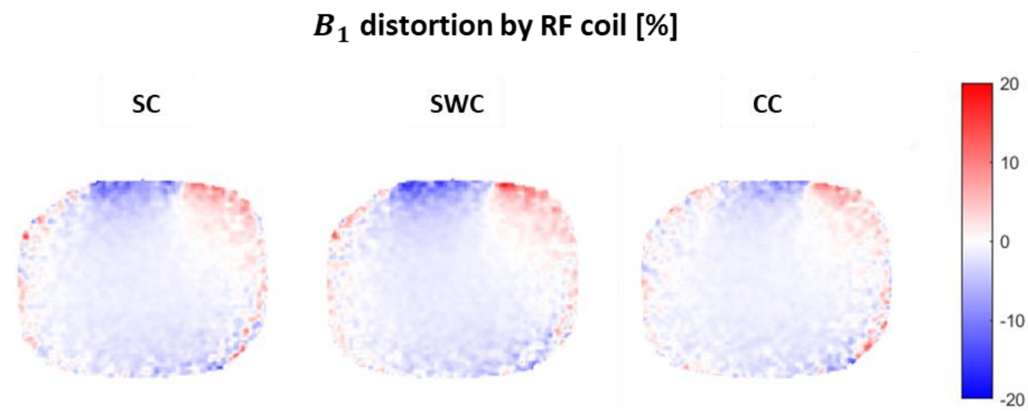

Fig. 4.3: B_1 distortion with vs. without coil in flat configuration of the SC, SWC, and CC. The scale covers a range from -20 to +20 % change when compared to the reference scan.

coil type	min. B_1 change [%]	max. B_1 change [%]
SC	-12.4	13.5
SWC	-16.1	18.2
CC	-15.9	13.3

Tab. 4.7: Minimal and maximal values of the B_1 change for every measured coil type in %.

4.1.2.2 Bent configuration

SNR

The three coils were measured in bent configuration using the balloon phantom as described in Subsection 3.6.1.1. Their SNR maps are presented in Fig. 4.4 and the absolute and relative values in the defined ROI are summarized in Tab. 4.8. The SNR profile along the central axis with increasing distance to the coil is plotted in Fig. 4.5. It indicates that the SC, which was not form fitted to the phantom, only has the highest SNR in a small region close to the coil. Above approximately 1.5 cm distance to the coil, the SWC showed higher SNR. The CC had a slightly lower SNR than the others, regardless of the distance to the coil.

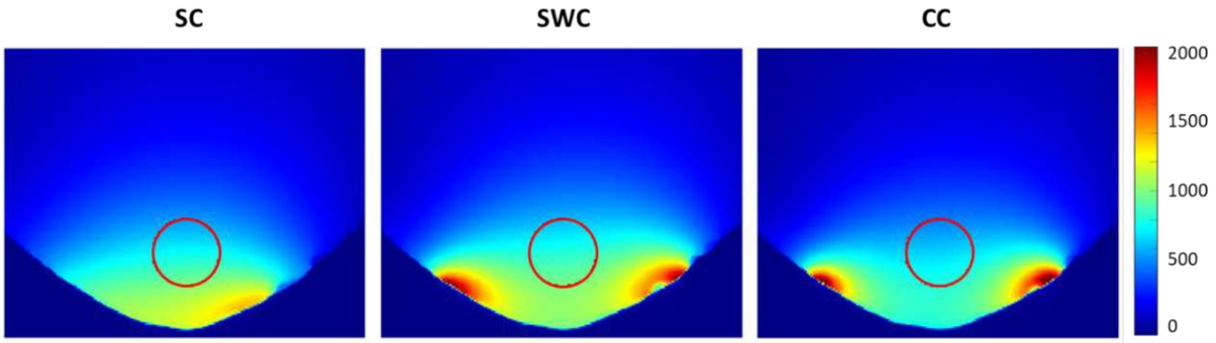

Fig. 4.4: SNR maps calculated from GRE of a transversal slice of the SC, SWC, and CC in bent configuration. The images are cropped images, and the red circle represents the ROI.

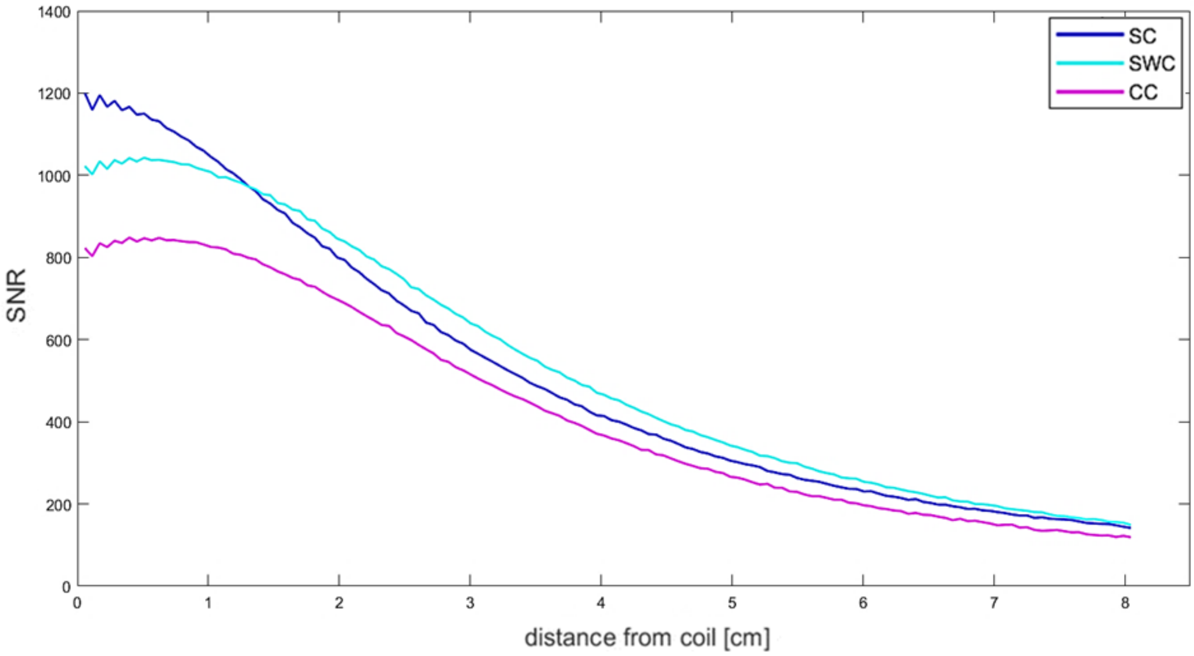

Fig. 4.5: SNR profile of the SC, SWC, and CC along the central axis in dependence of the distance to the respective coil.

coil type	SNR	vs. SC [%]
SC	786	-
SWC	836	+6.24
CC	685	-12.93

Tab. 4.8: Absolute values of the SNR in the region of interest of the SWC, CC, and SC and relative comparison of the SWC and CC to the SC.

B_1 distortion

The B_1 change can be seen in Fig. 4.6 and shows similar results to the flat measurements. The SWC had the highest decoupling from the body coil, nevertheless the SC and CC also demonstrated a sufficient active detuning network, remaining in a range of ± 16 % deviation from the reference scan. The minimum and maximum values of the B_1-change are shown in Tab. 4.9.

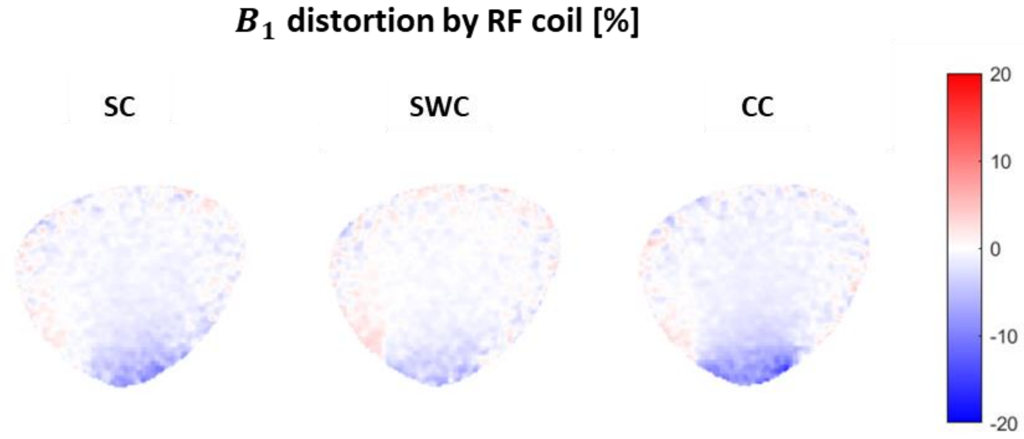

Fig. 4.6: B_1 distortion with vs. without coil in bent configuration of the SC, SWC, and CC. The scale covers a range from +20 to -20 % change when compared to the reference scan.

coil type	min. B_1 change [%]	max. B_1 change [%]
SC	-10.2	6.3
SWC	-8.2	5.1
CC	-16.0	4.2

Tab. 4.9: Minimal and maximal values of the B_1 change of the three coil types.

4.2 4-channel coil comparison

4.2.1 Bench measurements

The SWC and CC array were measured in flat configuration on top of the 5 liter tank phantom on the VNA as described in Subsection 3.5.8. The results of these bench measurements are listed in Tab. 4.10. The arrays showed similar Q-factors and the matching level remained below -14 dB for all channels.

	channel	Q-factor	$-S_{11}$ [dB]
SWC	**1**	12.7	16.3
	2	16.2	19.0
	3	13.9	28.9
	4	15.7	15.5
	channel	**Q-factor**	**$-S_{11}$ [dB]**
CC	**1**	16.2	14.3
	2	15.5	32.5
	3	19.9	22.5
	4	16.1	15.5

Tab. 4.10: Bench measurements of the SWC and CC array in flat configuration. The Q-factor and the matching level (S_{11}-parameter) of each channel at 123.2 MHz are shown.

Geometric decoupling

The S_{21} measurements were performed as described in Subsection 3.5.6 for the SWC and CC array. The results are summarized in Tab. 4.11. The coupling parameters S_{IJ} was below -9 dB between all channels for both the SWC and CC array. The coupling between channel 1 and 3 is relatively high for both arrays which can be explained by the arrangement of the coils: coil 1 and 3 are not overlapping in contrast to the others, which exploit geometric decoupling at the optimal overlap. The measurements revealed similar inter-element coupling for the two arrays.

SWC

ch	1	2	3
2	-11.2		
3	-9.0	-14.1	
4	-33.9	-11.3	-13.9

CC

ch	1	2	3
2	-13.7		
3	-9.1	-17.2	
4	-11.1	-10.7	-13.5

Tab. 4.11: Coupling parameters S_{IJ} [dB] between the coil elements of the SWC and CC array.

Preamplifier decoupling

The results of the measurement of the preamplifier decoupling, described in Subsection 3.5.6, are summarized in Tab. 4.12 for both coil arrays. It shows a slightly higher decoupling of the SWC array than the CC array. S_{21} differences below 9 dB were found for all channels of the two coil arrays.

SWC ch	Δ S_{21} [dB]
1	15.3
2	13.5
3	14.3
4	18.8

CC ch	Δ S_{21} [dB]
1	12.9
2	14.5
3	12.5
4	9.6

Tab. 4.12: Absolute difference between the S_{21} signals when connected to powered preamplifier vs. 50 Ω termination of the SWC and CC array.

4.2.2 MRI experiments

4.2.2.1 Comparison of the preamplifiers

The CC array was both measured with the smaller MwT and the HI-Q.A. preamplifiers. The SNR maps of a coronal slice of these two scans can be seen in Fig. 4.7. In the cylindric ROI, comparable SNR between the two amplifier types was measured. The SNR of the CC with the MwT preamplifiers was about 9 % higher.

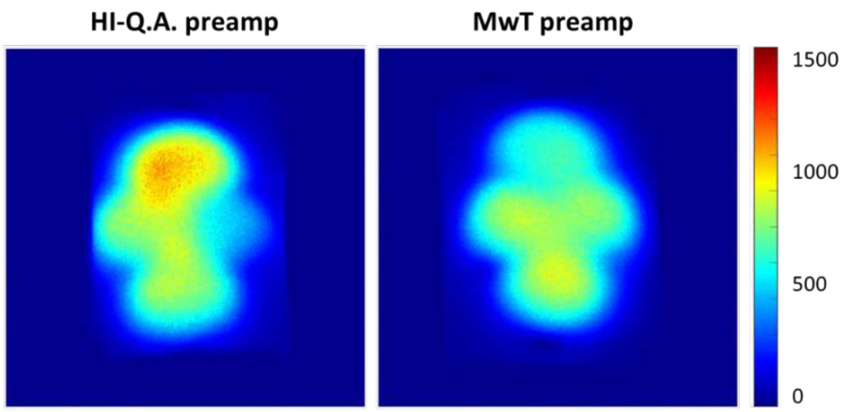

Fig. 4.7: SNR maps calculated from GRE of a coronal slice of the CC array using the HI-Q.A. and MwT preamplifiers.

4.2.2.2 SWC vs. CC

SNR

The results of the MR scans of the two arrays using a GRE sequence can be seen in Fig. 4.8 showing an overview of the SNR maps of a coronal, sagittal and transversal slice. Additional slices of the three orientations can be seen in Fig. 4.9, Fig. 4.10, and Fig. 4.11. An approximately 13 % higher SNR was found for the CC array in the defined cylindrical ROI using the MR scans in coronal orientation. Especially for the SWC array, a slightly uneven SNR distribution is noticeable in the coronal slices.

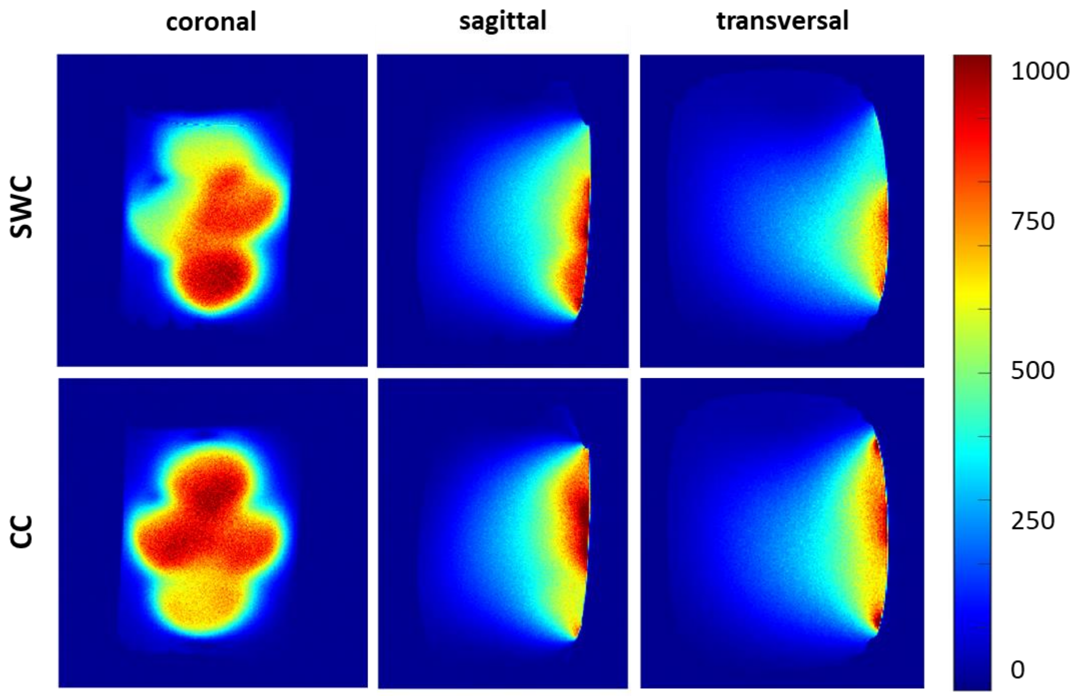

Fig. 4.8: SNR maps of the SWC and CC array calculated from coronal, sagittal, and transversal GRE scans. The central sagittal and transversal slices are shown, the coronal slice was measured in a depth of about 15 mm under the surface of the phantom.

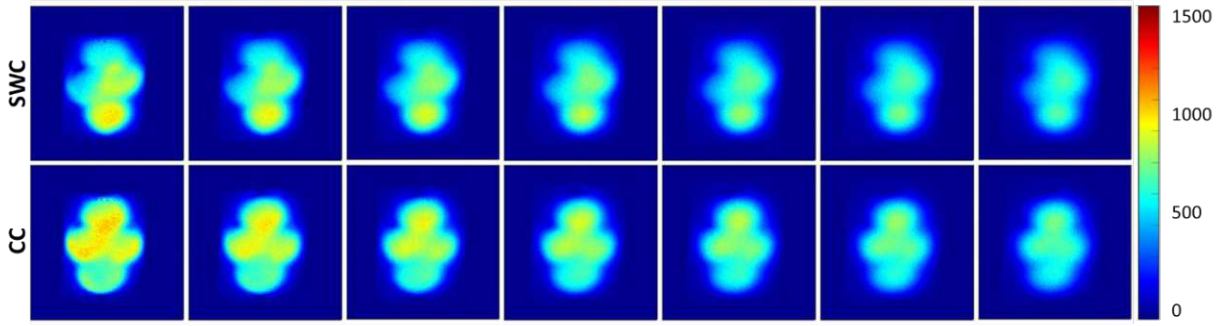

Fig. 4.9: SNR maps of the SWC and CC array calculated from coronal GRE measurements. The slice closest to the coil (left) was measured in a depth of about 15 mm under the surface of the phantom.

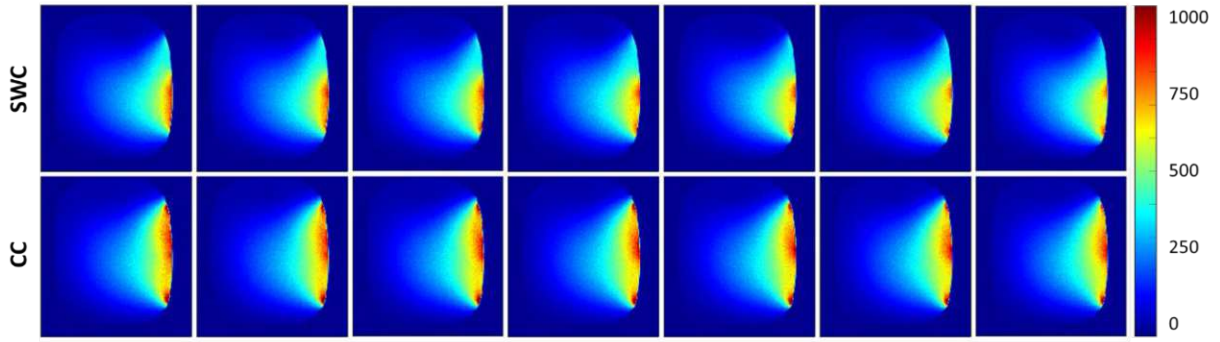

Fig. 4.10: SNR maps of the SWC and CC array calculated from transversal GRE measurements.

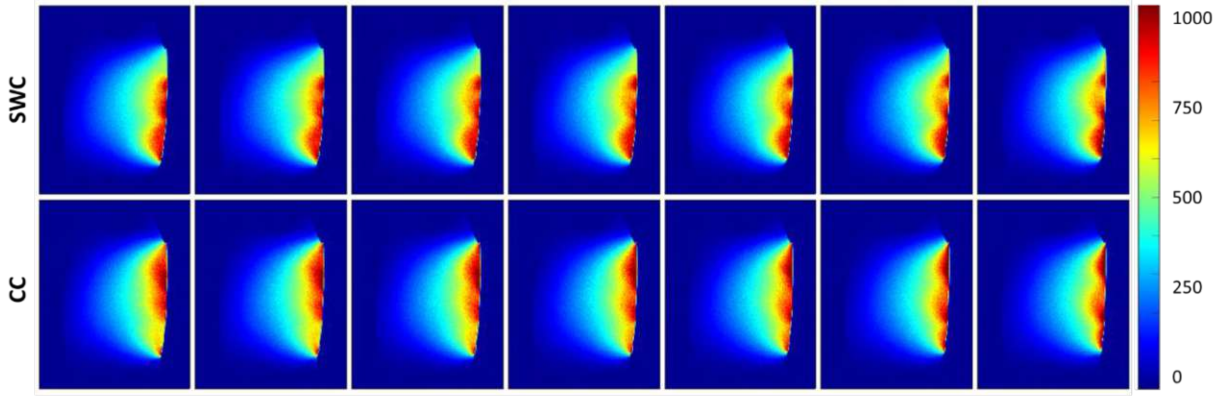

Fig. 4.11: SNR maps of the SWC and CC array calculated from sagittal GRE measurements.

B_1 distortion

The change of the B_1 field inside the phantom due to the presence of the SWC and CC array is shown in Fig. 4.12. It shows a central sagittal slice and a coronal slice about 12 mm under the surface of the phantom. Only directly beneath the respective coil, a stronger B_1 distortion is noticeable. This distortion declines significantly after about 1 cm into the phantom. The values of minimal and maximal B_1 change can be seen in Tab. 4.13. In the coronal slice the change stays between ± 28 % for both coil arrays.

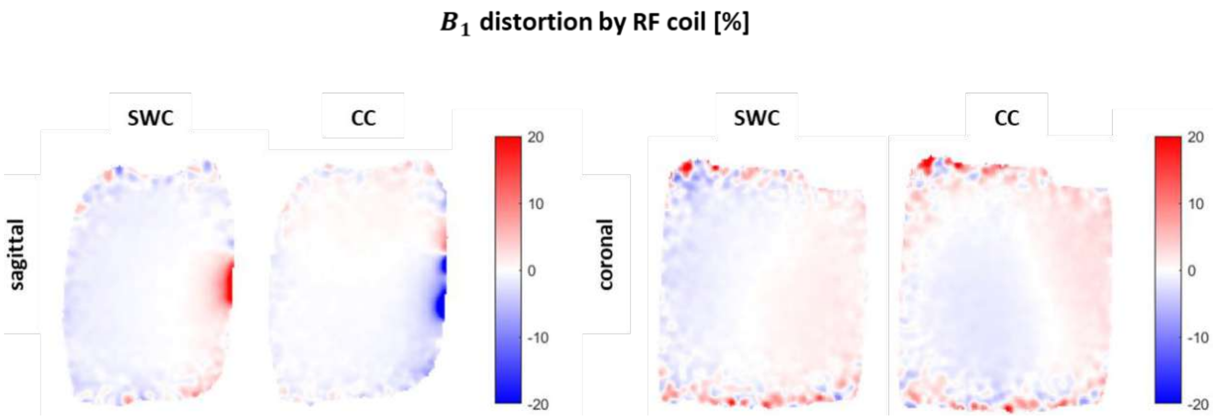

Fig. 4.12: Change of the B_1 field with vs. without the 4-channel SWC and CC. Central sagittal slices (left) and coronal slices about 2 cm under the respective coil (right) are shown.

coil/orientation	min. B_1 change [%]	max. B_1 change [%]
SWC/coronal	-11.0	26.7
CC/coronal	-8.1	27.7
SWC/sagittal	-10.6	25.3
CC/sagittal	-58.5	10.6

Tab. 4.13: Minimal and maximal B_1 distortion with vs. without coil of the SWC and CC array in coronal and sagittal orientation.

Noise correlation

The noise correlation matrix, describing the inter-element coupling, was calculated from the noise-only scan. The results of the two coil arrays are visualized in Fig. 4.13. Highest correlation was found between the elements 2 and 4 for the SWC with 39 %, and elements 1 and 3 for the CC with 35 %. The mean noise correlation of the SWC is slightly higher with 20.9 % than for the CC with 19.1 %.

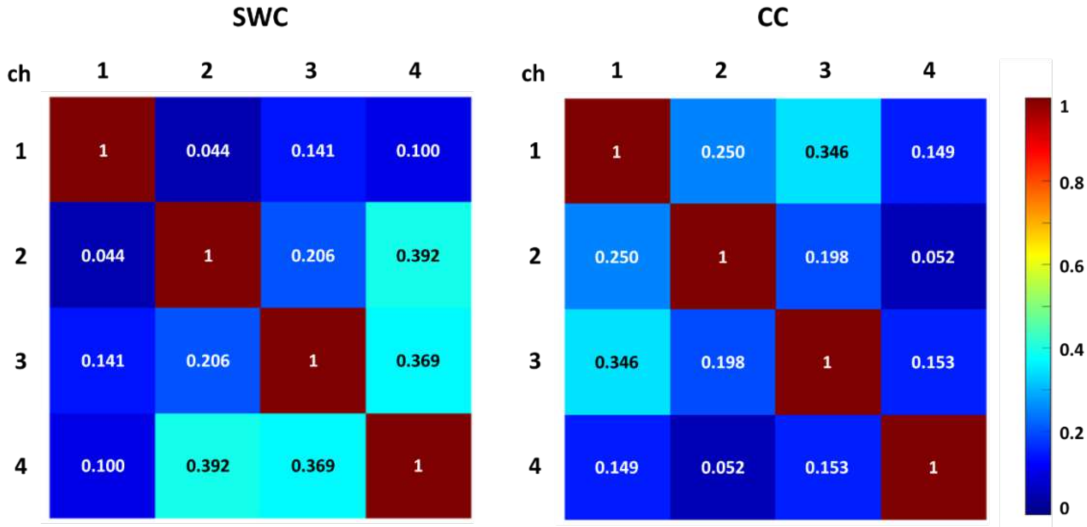

Fig. 4.13: Noise correlation matrix of SWC and CC. The matrix indices reach from channel 1 to channel 4 on both sides. The scale limits are 0 (lowest correlation) to 1 (highest correlation).

g-factor

The g-factor maps were calculated as described in Subsection 3.6.2.2 and can be seen in Fig. 4.14 for the SWC and CC array with an acceleration factor R = 2. A slice about 2 cm underneath the respective coil array can be seen. The direction of phase encoding and therefore, acceleration is from right to left. The g-factor remains low in the regions close to the respective coil. Higher g-factor values were found for the SWC, especially in two regions on the upper half of the phantom.

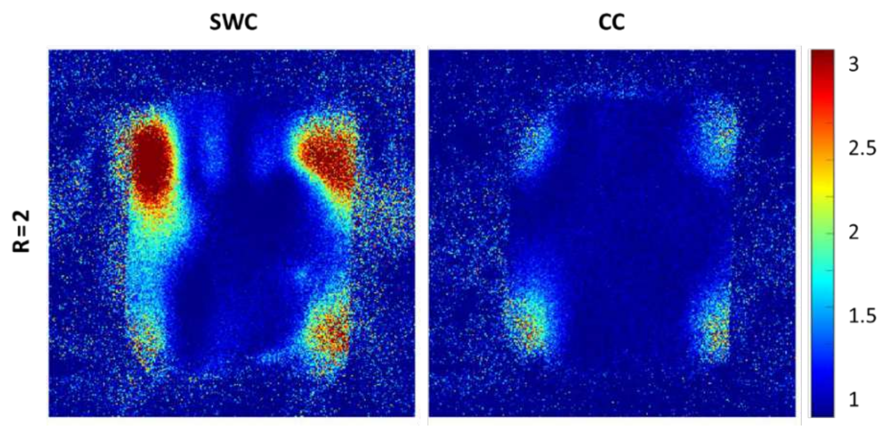

Fig. 4.14: g-factor maps of the SWC and CC array for an acceleration factor of R = 2 with phase encoding direction from right to left. The slice is about 2 cm under the respective coil.

5 Discussion and conclusion

Part of the methods and results of this work were presented during the international MR conference ISMRM 29th Annual Meeting & Exhibition 2021. The title of the abstract accepted for presentation is:

R. Czerny, M. Obermann, E. Laistler: "Performance of flexible coaxial transmission line resonators vs. stranded wire coils at 3 T"

5.1 Discussion

For the comparison of the investigated coil designs, various aspects must be considered. The physical behavior of flexible stranded wire coils is identical to standard loop coils. Both are tuned by capacitors soldered onto the conductor loop. On the contrary, coaxial transmission line resonators are self-resonant and tuned by the coil geometry and cable characteristics.

While both coil designs fulfill the requirement of mechanical flexibility, the CC showed higher robustness as no additional soldering joints for tuning capacitors are necessary. This is especially important for clinical use where frequent bending could lead to breakage of rigid parts on the coil such as the soldering joints. Nevertheless, standard interfacing technology can be used for SWCs.

VNA measurements showed differences between the single element coils with respect to coil noise. Lower unloaded Q-factors and thus Q-ratios were found for the CC in comparison to the other coil designs, indicating higher coil losses. Nevertheless, all coils were clearly sample noise dominated. GRE scans of the flexible SWC and CC only had slight SNR losses compared to the rigid SC (-4 % and -9%) in a circular ROI on the flat phantom, while allowing for form-fitting to the sample.

The comparison between the SWC and CC 4-channel array on the bench revealed similar inter-element coupling and preamplifier decoupling. MR measurements showed very similar SNR performance of both arrays. A slightly higher SNR was found in the cylindrical ROI for the CC array (+ 13 %). However, this might be partly caused by the use of different preamplifiers, which were found to slightly increase the SNR of the CC (+ 9 %). Considering these findings, it can be concluded that the two arrays have very similar SNR. The coronal SNR maps show an uneven distribution between coil channels, especially for the SWC array. Possible explanations might be a stronger coupling between certain channels. Slight tilting of the slices (away from parallel alignment with the plane of the array) on the scanner can also amplify this effect. In the central sagittal and transversal slices, the distribution of the SNR suggests that the array was not placed perfectly in the middle. Besides imperfections of the setup, another reason might be the deviation from symmetric overlap due to the optimization of the geometric decoupling. Differences of the SNR between the two arrays are possibly a combination of coil resistance and conductivity variances, small geometrical deviances, differences in the interfacing circuitry and electrical components (*e.g.*, preamplifiers) and noise correlation between coil channels. The noise correlation between coil channels was slightly lower for the CC array.

5.2 Conclusion

In this work, the successful development and implementation of a stranded wire receive coil array is shown. A performance comparison between this coil design and coaxial transmission line resonators is presented. The most important criteria were the mechanical flexibility and the achievable SNR performance. It was found that, while both are robust against bending in terms of frequency shifting, the solder joints along the conductor of the SWC represents a possible breaking point. Only a slightly lower SNR than for rigid standard coils was found for the flexible single channel coils on a flat phantom.

The 4-channel SWC and CC arrays performed similarly in terms of SNR. Slight differences were measured due to coil specific losses, different electrical components, and variances in the noise correlation between channels, among other causes.

To sum up, the choice between SWC and CC will be governed by practical considerations like the frequency and intensity of the bending of the coil, where the robustness of the CC outperforms the SWC due to potential breakage of solder joints.

5.3 Outlook

Further development of stranded wire coils could include the adaption of the rigid solder joints which is a drawback of this coil type. Soldering the capacitors onto small circuit boards, as described in this work, might not be the best choice regarding mechanical robustness. Finding a different approach to connect the capacitors onto the conductor without leaving a rigid area, could enhance the flexibility.

As the two coil designs showed similar SNR performance, the development of the “Bracoil” was continued using coaxial coils. This 28-channel breast coil for 3 T MRI will consist of multiple 4-channel CC arrays, arranged to cover the whole breast area. Due to the hexagonal layout, several 4-channel arrays can easily be assembled together in a modular fashion, without having to compromise the optimal overlap for geometric decoupling. With the high flexibility of these arrays, the “one-coil-fits-all” criteria can be fulfilled, enabling minimal distance to the measured body region. This allows for higher sensitivity, as well as higher patient comfort. MR measurements and bench tests of the Bracoil are currently conducted with further patient studies in planning.

6 References

[1] I. I. Rabi, J. R. Zacharias, S. Millman, and P. Kusch, “A New Method of Measuring Nuclear Magnetic Moment,” *American Physical Society*, vol. 53, no. 4, p. 318, 1938.

[2] F. Bloch, W. E. Hansen, and M. Packard, “The Nuclear Induction Experiment,” *Physical Review*, vol. 70, no. 7–8, pp. 474–485, 1946.

[3] E. M. Purcell, H. C. Torrey, and R. V. Pound, “Resonance Absorption by Nucelar Magnetic Moments in a Solid,” *Physical Review*, vol. 69, no. 1–2, pp. 37–38, 1946.

[4] E. M. Haacke, R. W. Brown, R. Venkatesan, M. R. Thompson, and Y.-C. N. Cheng, *Magentic Resonance Imaging: Physical Principles and Sequence Design*. Hoboken: John Wiley & Sons, INC., 1999.

[5] M. Woytasik *et al.*, “Characterization of flexible RF microcoils dedicated to local MRI,” *Microsystem Technologies*, vol. 13, no. 11–12, pp. 1575–1580, 2006.

[6] E. Laistler and E. Moser, “Handy magnetic resonance coils,” *Nature Biomedical Engineering*, vol. 2, pp. 557–558, 2018.

[7] W. Demtröder, *Experimentalphysik 3: Atome, Moleküle und Festkörper*, Edition 5., Berlin, Heidelberg: Springer-Verlag, 2016.

[8] M. F. Reiser, W. Semmler, and H. Hricak, *Magnetic Resonance Tomography*, Edition 3., Berlin, Heidelberg: Springer-Verlag, 2002.

[9] R. Kriegl, “A flexible coil array for high resolution magnetic resonance imaging at 7 Tesla,” Ph.D. thesis, Medical University of Vienna and Université Paris Sud, 2014.

[10] S. Goluch, “A design and development procedure for transceive radio frequency coils in ultra-high field magnetic resonance,” Ph.D. thesis, Medical University of Vienna, 2015.

[11] W. Demtröder, *Experimentalphysik 2: Elektrizität und Optik*, Edition 3., Berlin, Heidelberg: Springer-Verlag, 2004.

[12] V. Kuperman, *Magnetic Resonance Imaging: Physical Principles and Applications*. San Diego: Academic Press, 2000.

[13] A. C. Özen, *Novel MRI Technologies for Structural and Functional Imaging of Tissues with Ultra-short* T_2, Karlsruhe: KIT Scientific Publishing, 2017.

[14] L. Darrasse and J. C. Ginefri, “Perspectives with cryogenic RF probes in biomedical MRI,” *Biochimie*, vol. 85, pp. 915–937, 2003.

[15] M. Obermann, “An ultra-flexible 3-channel receive-only coil array for 3T magnetic resonance imaging made of coaxial transmission line resonators,” diploma thesis, Vienna University of Technology, 2018.

[16] L. Nohava *et al.*, “Flexible multi-turn multi-gap coaxial RF coils: design concept and implementation for Magnetic Resonance Imaging at 3 and 7 Tesla,” *IEEE Transactions on Medical Imaging*, vol. 40, no. 4, pp. 1267–1278, 2021.

[17] J. Mispelter, M. Lupu, and A. Briguet, *NMR Probeheads for Biophysical and Biomedical Experiments: Theoretical Principles and Practical Guidelines*. London: Imperial College Press, 2006.

[18] P. B. Roemer, W. A. Edelstein, C. E. Hayes, S. P. Souza, and O. M. Mueller, “The NMR Phased Array,” *Magnetic Resonance in Medicine*, vol. 16, pp. 192–225, 1990.

[19] A. Reykowski, S. M. Wright, and J. R. Porter, “Design of Matching Networks for Low Noise Preamplifiers,” *Magnetic Resonance in Medicine*, vol. 33, no. 6, pp. 848–852, 1995.

[20] G. P. Srivastava and V. L. Gupta, *Microwave Devices and Circuit Design*. Delhi: PHI Learning, 2006.

[21] J. T. Vaughan and J. R. Griffiths, *RF coils for MRI*. Chichester, West Sussex: John Wiley & Sons, INC., 2012.

[22] P. Gonord, S. Kan, and A. Leroy-Willig, “Parallel-plate split-conductor surface coil: Analysis and design,” *Magnetic Resonance in Medicine*, vol. 6, no. 353–358, 1988.

[23] P. Gonord, S. Kan, A. Leroy-Willig, and C. Wary, “Multigap parallel-plate bracelet resonator frequency determination and applications,” *Review of Scientific Instruments*, vol. 65, no. 11, pp. 353–358, 1994.

[24] R. Kriegl *et al.*, “Novel inductive decoupling technique for flexible transceiver arrays of monolithic transmission line resonators,” *Magnetic Resonance in Medicine*, vol. 73, pp. 1669–1681, 2015.

[25] R. Frass-Kriegl *et al.*, “Multi-turn multi-gap transmission line resonators - Concept, design and first implementation at 4.7T and 7T,” *Journal of Magnetic Resonance*, vol. 273, pp. 65–72, 2016.

[26] S. Serfaty, N. Haziza, L. Darrasse, and S. Kan, “Multi-Turn Split-Conductor Transmission-Line Resonators,” *Magnetic Resonance in Medicine*, vol. 38, pp. 687–689, 1997.

[27] B. Zhang, D. K. Sodickson, and M. A. Cloos, “A high-impedance detector-array glove for magnetic resonance imaging of the hand,” *Nature Biomedical Engineering*, vol. 2, pp. 570–577, 2018.

[28] X. Yang, T. Zheng, Y. Wu, and M. Finnerty, “Coaxial cable magnetic resonance image (MRI) coils,” US patent US9678180B2, 2017.

[29] M. S. M. Mollaei, C. C. van Leeuwen, A. J. E. Raaijmakers, and C. Simovski, “Analysis of High Impedance Coils both in Transmission and Reception Regimes,” *IEEE Access*, vol. 8, pp. 129754–129762, 2020.

[30] I. Zivkovic, T. Ruytenberg, and A. Webb, “Shielded-coaxial-cable coils as receive and transceive array elements for 7T human MRI,” *Magnetic Resonance in Medicine*, vol. 83, no. 3, pp. 1135–1146, 2020.

[31] M. Obermann *et al.*, “Ultra-flexible and light-weight 3-channel coaxial transmission line resonator receive-only coil array for 3T,” in *Proc. 27th Int. Soc. Magn. Reson. Med.*, Montréal, Canada, p. 1558, 2019.

[32] D. K. Sodickson and W. J. Manning, “Simultaneous acquisition of spatial harmonics (SMASH): Fast imaging with radiofrequency coil arrays,” *Magnetic Resonance in Medicine*, vol. 38(4), pp. 591–603, 1997.

[33] K. P. Pruessmann, M. Weiger, M. B. Scheidegger, and P. Boesiger, “SENSE: Sensitivity Encoding for Fast MRI,” *Magnetic Resonance in Medicine*, vol. 42, pp. 952–962, 1999.

[34] M. A. Griswold *et al.*, “Generalized autocalibrating partially parallel acquisitions (GRAPPA),” *Magnetic Resonance in Medicine*, vol. 47, pp. 1202–1210, 2002.

[35] J. A. Nordmeyer-Massner, N. De Zanche, and K. P. Pruessmann, “Stretchable coil arrays: Application to knee imaging under varying flexion angles,” *Magnetic Resonance in Medicine*, vol. 67, pp. 872–879, 2012.

[36] A. Port *et al.*, “Liquid metal in stretchable tubes: A wearable 4-channel knee array,” in *Proc. 27th Int. Soc. Magn. Reson. Med.*, Montréal, Canada, p. 1114, 2019.

[37] B. Zhang, D. K. Sodickson, and M. A. Cloos, “A high-impedance detector-array glove for magnetic resonance imaging of the hand,” *Nature Biomedical Engineering*, vol. 2, pp. 570–577, 2018.

[38] S. Roat, M. Vít, S. Wampl, A. I. Schmid, and E. Laistler, “A Flexible Array for Cardiac 31P MR Spectroscopy at 7 T,” *Frontiers in Physics*, vol. 8, 2020.

[39] P. M. Robson, A. K. Grant, A. J. Madhuranthakam, R. Lattanzi, D. K. Sodickson, and C. A. McKenzie, “Comprehensive quantification of signal-to-noise ratio and g-factor for image-based and k-space-based parallel imaging reconstructions,” *Magnetic Resonance in Medicine*, vol. 60, no. 4, pp. 895–907, 2008.

[40] Microwaves101, “High-Pass Low-Pass Phase Shifters.” https://www.microwaves101.com/encyclopedias/high-pass-low-pass-phase-shifters (accessed Apr. 02, 2020).

[41] R. B. Lauffer, “Paramagnetic Metal Complexes as Water Proton Relaxation Agents for NMR Imaging: Therory and Design,” *Chem. Rev.*, vol. 87, pp. 901–927, 1987.

[42] J. Mispelter, M. Lupu, and A. Briguet, *NMR Probeheads for Biophysical and Biomedical Experiments: Theoretical Principles and Practical Guidelines*. London: Imperial College Press, 2006.

[43] D. A. Seeber, J. Jevtic, and A. Menon, “Floating shield current suppression trap,” *Concepts in Magnetic Resonance Part B: Magnetic Resonance Engineering*, vol. 21, no. 1, pp. 26–31, 2004.

[44] M. Sayed, A. Ferrero, and V. Teppati, *Modern RF and Microwave Measurement Techniques*. New York: Cambridge University Press, 2013.

[45] L. Darrasse and G. Kassab, “Quick measurement of NMR-coil sensitivity with a dual-loop probe,” *Review of Scientific Instruments*, vol. 64, pp. 1841–1844, 1993.

7 List of Figures

8 List of Tables